Neurobiology of Disease 180 (2023) 106083

Contents lists available at ScienceDirect

Neurobiology of Disease

journal homepage: www.elsevier.com/locate/ynbdi

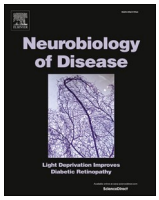

A comprehensive longitudinal study of magnetic resonance imaging identifies novel features of the *Mecp2* deficient mouse brain

Sara Carli [a,1,2], Linda Chaabane [b,3,1], Giuseppina De Rocco [a,c], Elena Albizzati [c,4], Irene Sormonta [a], Stefano Calligaro [a], Pietro Bonizzi [d], Angelisa Frasca [c], Nicoletta Landsberger [a,c,*]

[a] *Neuroscience Division, IRCCS San Raffaele Scientific Institute, Milan I-20132, Italy*
[b] *Institute of Experimental Neurology (INSPE) and Experimental Imaging Center (CIS), IRCCS San Raffaele Scientific Institute, Milan I-20132, Italy*
[c] *Department of Medical Biotechnology and Translational Medicine, University of Milan, Segrate (Milan) I-20090, Italy*
[d] *Department of Advanced Computing Sciences, Maastricht University, Maastricht, the Netherlands*

A R T I C L E I N F O

Keywords:
Rett syndrome (RTT)
Mecp2 mouse models
In vivo MRI/MRS studies
Biomarkers
Neurodevelopment
Neuroimaging

A B S T R A C T

Rett syndrome (RTT) is a X-linked neurodevelopmental disorder which represents the leading cause of severe incurable intellectual disability in females worldwide. The vast majority of RTT cases are caused by mutations in the X-linked *MECP2* gene, and preclinical studies on RTT largely benefit from the use of mouse models of *Mecp2*, which present a broad spectrum of symptoms phenocopying those manifested by RTT patients.

Neurons represent the core targets of the pathology; however, neuroanatomical abnormalities that regionally characterize the *Mecp2* deficient mammalian brain remain ill-defined.

Neuroimaging techniques, such as MRI and MRS, represent a key approach for assessing *in vivo* anatomic and metabolic changes in brain. Being non-invasive, these analyses also permit to investigate how the disease progresses over time through longitudinal studies.

To foster the biological comprehension of RTT and identify useful biomarkers, we have performed a thorough *in vivo* longitudinal study of MRI and MRS in *Mecp2* deficient mouse brains. Analyses were performed on both genders of two different mouse models of RTT, using an automatic atlas-based segmentation tool that permitted to obtain a detailed and unbiased description of the whole RTT mouse brain. We found that the most robust alteration of the RTT brain consists in an overall reduction of the brain volume. Accordingly, *Mecp2* deficiency generally delays brain growth, eventually leading, in heterozygous older animals, to stagnation and/or contraction. Most but not all brain regions participate in the observed deficiency in brain size; similarly, the volumetric defect progresses diversely in different brain areas also depending on the specific *Mecp2* genetic lesion and gender. Interestingly, in some regions volumetric defects anticipate overt symptoms, possibly revealing where the pathology originates and providing a useful biomarker for assessing drug efficacy in preclinical studies.

* Corresponding author at: Department of Medical Biotechnology and Translational Medicine, University of Milan, Segrate (Milan) I-20090, Italy.
E-mail addresses: sara.carli4@unibo.it (S. Carli), linda.chaabane@cnr.it (L. Chaabane), giuseppina.derocco@unimi.it (G. De Rocco), Elena.Albizzati@cchmc.org (E. Albizzati), sormonta.irene@hsr.it (I. Sormonta), calligaro.stefano@hsr.it (S. Calligaro), pietro.bonizzi@maastrichtuniversity.nl (P. Bonizzi), angelisa.frasca@unimi.it (A. Frasca), nicoletta.landsberger@unimi.it, landsberger.nicoletta@hsr.it (N. Landsberger).
[1] Sara Carli and Linda Chaabane contributed equally to this work.
[2] Center for Applied Biomedical Research, University of Bologna, Via Massarenti 9, 40138 Bologna, Italy; sara.carli4@unibo.it (S.C.) (ORCID 0000-0001-8130-5364).
[3] Euro-BioImaging ERIC, Institute of Biostructures and Bioimaging (IBB), Italian National Research Council (CNR), Via Nizza 52, Torino, 10126, Italy; linda.chaabane@cnr.it (L.C.) (ORCID 0000-0003-2782-9938).
[4] Division of Developmental Biology, Cincinnati Children's Hospital Medical Center, Cincinnati, OH 45229, USA; Elena.Albizzati@cchmc.org (E.A.).

https://doi.org/10.1016/j.nbd.2023.106083
Received 13 December 2022; Received in revised form 17 February 2023; Accepted 13 March 2023
Available online 15 March 2023

1. Introduction

Mutations in the X-linked *MECP2* gene coding for a well-known epigenetic transcriptional repressor cause Rett syndrome (RTT; OMIM 312750), a severe neurodevelopmental disorder, mainly affecting females. RTT patients show a delayed onset of apparent symptoms, whose identification still relies on clinical diagnosis (Neul et al., 2010). Indeed, they appear to have a normal development for the first 6–18 months of life, when their neurological development arrests. Then, a typical regression phase occurs, and the young patients lose most of the skills that they have previously acquired, such as learned words and babble, motor skills and purposeful hand use. In this phase, patients also acquire continuous and characteristic stereotypic hand movements, gait abnormalities and develop autistic features that, however, improve over the years. Conversely, with the progression of the disorder, patients accumulate several other symptoms; the most common and destructive include seizures, breathing abnormalities, severe scoliosis, hypotonia, autonomic dysfunctions, cardiac abnormalities, often featuring prolonged QT intervals, and acquired rigidity and Parkinsonian features (Borloz et al., 2021).

Importantly, and diversely from the usual perception, abnormalities are already present during early development. Indeed, atypical movements characterize RTT patients in the fetal and perinatal period while an abnormal deceleration in head growth, leading to microcephaly, generally appears within the first year of life (Cosentino et al., 2019; Marschik et al., 2013). Accordingly, the RTT brain derived from 4 to 12 years old patients is comparable to a healthy one-year old child brain and appears to remain stable for at least 4 decades of life, with no sign of neurodegeneration (Armstrong, 2001). Attempts to understand the main causes for microcephaly led to postulate the contribution of several factors, including defects in dendritic arborization and synaptic density, a reduction in neuronal soma size and augmented cell density (Belichenko et al., 2009).

The generation of several mouse models carrying different *Mecp2* mutations has been instrumental to increase the comprehension of MeCP2 functions and the mechanisms underpinning *MECP2*-related conditions (Lombardi et al., 2015). Their validity is proved by the presence of a broad spectrum of clinical and cellular phenotypes and some molecular alterations manifested by RTT patients (Bedogni et al., 2014; Calfa et al., 2011; Shovlin and Tropea, 2018). RTT patients generally harbor a missense, nonsense or frameshift *MECP2* mutation in a heterozygous state; however, most basic and preclinical studies have been performed on hemizygous male mice which present more robust, consistent and earlier phenotypes with respect to the female counterparts. In particular, *Mecp2* KO mice have no apparent symptom up to almost 30 days of age when gross abnormalities appear with a rapid worsening, and premature death generally occurs within 8 to 11 weeks of age (Calfa et al., 2011; Frasca et al., 2023). *Mecp2* heterozygous female (HET) mice manifest similar but milder features that normally emerge in the first 3–4 months of life; in line with RTT patients, with an average life expectancy of 55 years, they generally survive >12 months (Frasca et al., 2023).

Remarkably, transcriptional defects are already present in the KO embryonic cerebral cortex, thus well before the onset of overt symptoms (Bedogni et al., 2016). Further, *Mecp2* conditional deletion at different postnatal ages (from juvenile to adult male mice) always leads to the appearance of typical RTT symptoms and premature death. Altogether, these results prove that MeCP2 expression and functions in mammalian brain are always required, both for proper neurodevelopment and for maintaining fully functional mature neurons (reviewed in Frasca et al., 2023).

Reduction in the whole brain size and weight has been reported in most *Mecp2* mutant mice (Saywell et al., 2006; Stearns et al., 2007; Ward et al., 2008, 2009). In particular, through Magnetic Resonance Imaging (MRI), Saywell and colleagues proved that 5–8 weeks old KO male mice feature the expected global reduction in brain size (Saywell et al., 2006). As for RTT patients, cerebral reduction mainly affects specific brain areas, such as motor cortex and corpus callosum. Histological analyses in young KO mice (P35) confirmed regional differences in volume reduction (Stearns et al., 2007). In order to understand when and where anatomical deficits appear, Ward and colleagues used longitudinal MRI (from P21 to P42) to track the development of the whole brain together with few specific areas in KO and HET mice (Ward et al., 2008). This study suggested that brain volume reduction emerges already at early time points and females manifest more modest defects. Notably, NMR spectroscopy was also used at the same ages to compare the levels of different metabolites in WT and *Mecp2* defective brains, revealing lower levels of choline, *N*-acetyl aspartate and glutamate to glutamine ratio in mutant animals (Ward et al., 2009).

To determine the effect of different *Mecp2* mutations, a more recent MRI study compared *ex vivo* the brain of the *Mecp2*^{308} model, that harbors a late STOP codon and features mild symptoms, with the *Mecp2*$^{tm1.1Bird}$ null line (Allemang-Grand et al., 2017; Guy et al., 2001; Shahbazian et al., 2002). A deep analysis of the whole brain structures, that included 159 segmented regions examined in P200 females and P60 males, revealed that striatum, thalamus and white matter tracts, together with several cortical regions, were smaller in all mutant animals, with major differences in mice having a more severe genetic lesion. Since no interaction between sex and genotype was observed, the authors suggested that hemizygous males provide a valid model for MRI studies (Allemang-Grand et al., 2017).

Overall, these published results confirmed the power of MRI for localizing and quantifying anatomical alterations in RTT brains and for associating them with disease severity.

A better comprehension of the pathological features that characterize the *Mecp2* deficient mouse brain might benefit from an *in vivo* longitudinal study detailing in several brain regions the progression of the disorder. To fill this gap of knowledge and possibly reconcile apparently discordant results, we analyzed both genders of the largely used *Mecp2*$^{tm1.1Bird}$ line (Guy et al., 2001) at different ages roughly corresponding to pre, early and late symptomatic phases, covering the whole brain, thus avoiding prior hypotheses of the mostly affected regions. Cerebral metabolism on selected areas was also analyzed by *in vivo* Magnetic Resonance Spectroscopy (MRS). To investigate to what extent the KO brain development might differ from that one of a severe knock-in (KI) mouse line mutated in the methyl DNA binding domain of the protein (Bedogni et al., 2016), we also performed a longitudinal study in the *Mecp2*^{Y120D} line that we have recently generated (Gandaglia et al., 2019).

2. Results

2.1. *Mecp2* deficient mouse brain exhibits a progressive reduction in overall volume

Neuroanatomical alterations of the *Mecp2* null brain were investigated during disease progression in hemizygous males and heterozygous females with respect to their corresponding WT littermates, starting from a generally defined pre-symptomatic time point, in which behavioral defects are not yet overt (P20 for males and P60 for females), to a barely symptomatic age (P30 for males and P90 for females) and a fully symptomatic stage (P40 for males and P200 for females). Symptoms were evaluated and scored as previously described (Cobolli Gigli et al., 2016) (Fig. 1A).

Quantitative morphometric analyses of MRI data were done on all animals using a widely used advanced and unbiased automatic atlas-based segmentation tool (ANTx2, open-source software) that allowed the discrimination of all mice cerebral areas (Koch et al., 2019). Longitudinal MRI confirmed the expected reduction in cerebral volume in *Mecp2* deficient mice of both genders (Fig. 1B). Indeed, the P20 KO male brain volume exhibited a trend to decrement with respect to the corresponding WT brains (WT: 0.413 ± 0.009 cm^3; KO: 0.393 ± 0.005 cm^3;

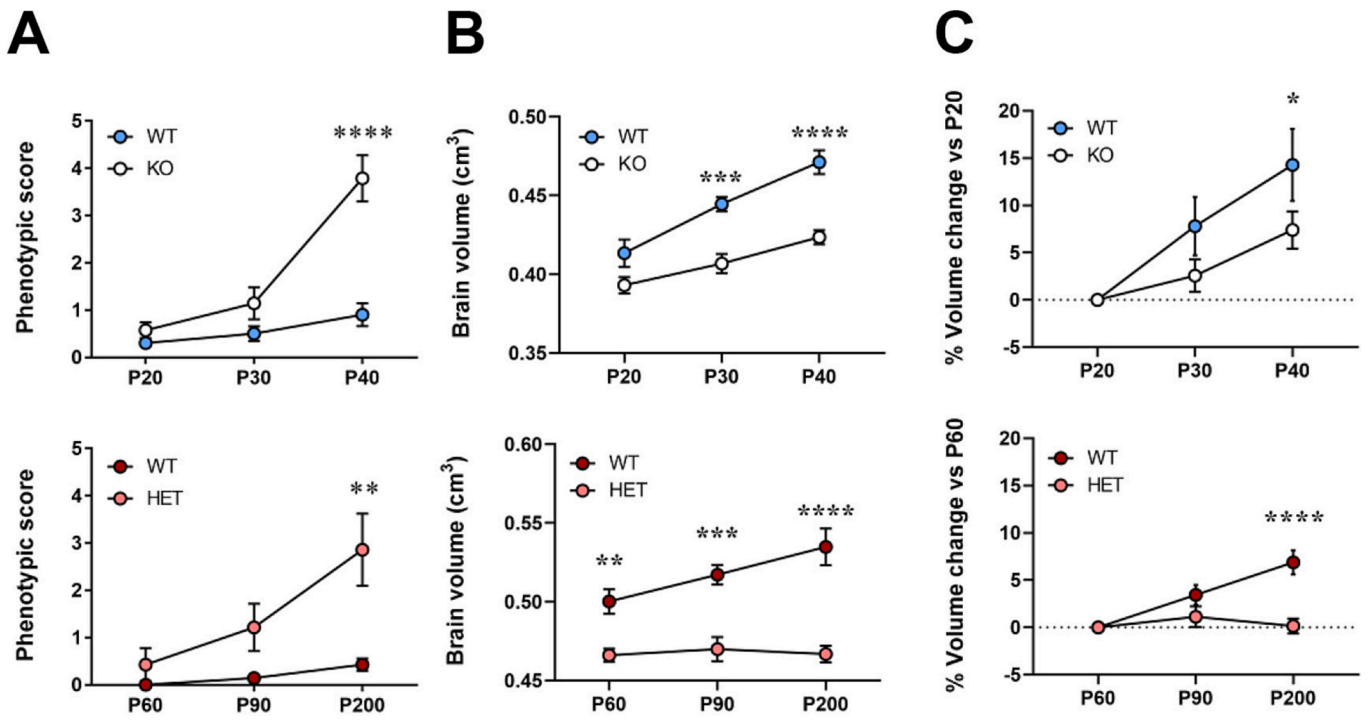

Fig. 1. (A) Graphs depict the progression of the phenotypic score, cumulated for general condition, mobility, hind limb clasping, and tremor in male (upper panel) and females (lower panel) mice from the *Mecp2*$^{tm1.1Bird}$ line. (B) *In vivo* longitudinal MRI shows a significant reduction in the total brain volume (cm^3) of *Mecp2* Bird animals of both genders. Male KO mice (upper panel) unveil a significant defect since P30, while female HET animals (lower panel) show a significant reduction of the brain volume at any time point of analysis. (C) Growth trajectory of the brain volume progression in comparison to the first time point of analysis in *Mecp2* mutant males (upper panel) and females (lower panel). Male mice: WT, $n = 5$; KO, $n = 7$. Female mice WT, $n = 6$; HET, $n = 6$. Animals whose fitting in the segmentation was not optimal were excluded from the analysis. Each mutant mouse was evaluated in comparison to its WT littermates by Two-way repeated measures ANOVA or Mixed-Model Analysis, followed by Sidak post-hoc (A,B) or Fisher's LSD post-hoc (C); *$p < 0.05$; **$p < 0.01$; ***$p < 0.001$; ****$p < 0.0001$.

-4.9 ± 1.2% compared to WT, p value = 0.0876), while a significant difference was observed at P30 (WT: 0.445 ± 0.004 cm^3; KO: 0.407 ± 0.006 cm^3; −8.5 ± 1.4% compared to WT, p value = 0.0004) and reinforced at P40 (WT: 0.471 ± 0.008 cm^3; KO: 0.424 ± 0.004 cm^3; −10.1 ± 1.0% compared to WT, p value<0.0001). Interestingly, the HET brain was already significantly smaller at the apparently asymptomatic age of P60, with an evident worsening of the defect over time (P60: WT: 0.500 ± 0.008 cm^3; HET: 0.466 ± 0.004 cm^3; −6.8 ± 0.8% compared to WT, p value = 0.0083; P90: WT: 0.517 ± 0.006 cm^3; HET: 0.470 ± 0.008 cm^3; −9.1 ± 1.5%, p value = 0.0005; P200: WT: 0.535 ± 0.012 cm^3; HET: 0.467 ± 0.005 cm^3; −12.7 ± 1.0%, p value<0.0001). As highlighted by the percentage of brain volume change with respect to the first time point of analysis (P20 for males and P60 for females; Fig. 1C), the growth rate of KO brains was slower reaching a significant difference at the last time point (Fig. 1C, upper panel). In females, the volume of WT brains showed a minor but constant growth overtime, in line with their advanced age. Conversely, no growth was observed for the HET brains, therefore leading to a more solid defect at the last time point of analysis, indicative of growth stagnation (Fig. 1C, lower panel).

2.2. *In vivo longitudinal studies confirm a specific regional effect of Mecp2 deficiency in brain whose consequences vary depending on the gender*

To reveal how the disorder progresses in different brain regions and which structures are initially and/or mainly affected, a deep analysis was performed over all the collected MRI scans (Koch et al., 2019). >800 brain structures were determined and compared in *Mecp2* deficient male and female animals with respect to gender- and age-matched WT littermates (all raw data are reported in San Raffaele Open Research Data Repository (ORDR)). Initially, we focused on major brain areas (cerebral cortex, hippocampal formation, basal ganglia, interbrain, midbrain, hindbrain, cerebellum, corpus callosum and ventricular system) analyzing their development overtime. As shown in Table 1, at P20, some regions, including hippocampus, basal ganglia, interbrain and ventricular system, already featured a significant defect, although the overall KO brain volume was not yet significantly decreased compared to controls (Fig. 1B). At P30, all the analyzed structures revealed a significant volume reduction, except for the hindbrain, while at P40, all major regions shared roughly a 10% of decrement with respect to the WT counterparts. Interestingly, and in line with their role in higher cognitive functions, hippocampus and corpus callosum exhibited a strong volume reduction from P30 to P40, reaching a decrement of 14 and 12,5%, respectively.

Analysis of older HET females confirmed the progressive reduction of most of the analyzed structures, with the exception of the ventricular system that was constantly affected in both genders. Further, and diversely from KO mice, the heterozygous cerebellar size remained comparable to the WT one.

We continued by measuring the size of the relative subareas. Table 2 reports most relevant results. Among the analyzed cortical sub-regions, entorhinal, somatomotor and somatosensory cortex appeared as most affected in barely and fully symptomatic KO animals, and a contribution of visual cortex was also present at the last time point. Conversely, prefrontal cortex remained preserved. In HET females, cerebral cortex reduction seems to be mainly attributable to prefrontal, entorhinal and somatosensory cortices at P90 and to all analyzed sub-cortical regions at P200. Interestingly, at the latest time points of analyses, entorhinal cortex, which plays a major role in memory formation and consolidation, revealed the largest volume reduction in both genders (~14.5% in null males and 15.7% in HET females).

Analysis of the hippocampal sub-regions unveiled a diffuse alteration in CA1, CA3 and dentate gyrus, with a minor involvement of CA2 both in

Table 1
Volume difference (%) of KO and HET main brain areas compared to WT littermates.

Anatomical Region	Males %difference to WT (Mean ± SEM) [*p* value]			Females %difference to WT (Mean ± SEM) [p value]		
	P20	P30	P40	P60	P90	P200
Cerebral cortex	−5.1 ± 0.9 [0.3767]	−8.5 ± 2.1 **[0.0088]**	−10.4 ± 1.7 **[0.0007]**	−6.1 ± 0.9 [0.0534]	−8.4 ± 1.5 **[0.0063]**	−12.6 ± 1.3 [<**0.0001**]
Hippocampal area	−8.0 ± 1.0 **[0.0314]**	−10.9 ± 1.5 **[0.0006]**	−14.0 ± 2.1 **[<0.0001]**	−10.9 ± 1.6 **[0.0105]**	−13.9 ± 1.8 **[0.0010]**	−17.9 ± 1.5 **[<0.0001]**
Basal ganglia	−5.6 ± 0.7 **[0.0441]**	−8.1 ± 1.3 **[0.0007]**	−11.4 ± 0.8 **[<0.0001]**	−8.4 ± 0.5 **[0.0013]**	−9.6 ± 1.4 **[0.0004]**	−14.3 ± 1.0 **[<0.0001]**
Interbrain	−6.0 ± 1.8 **[0.0066]**	−9.6 ± 0.7 [<**0.0001**]	−9.7 ± 0.8 [<**0.0001**]	−7.8 ± 0.7 **[0.0010]**	−11.0 ± 1.2 **[<0.0001]**	−14.1 ± 1.0 **[<0.0001]**
Midbrain	−4.9 ± 1.8 [0.0861]	−7.4 ± 1.3 **[0.0016]**	−8.0 ± 0.9 **[0.0004]**	−8.1 ± 1.5 **[0.0037]**	−10.8 ± 1.5 **[0.0002]**	−12.1 ± 0.9 **[<0.0001]**
Hindbrain	−2.9 ± 2.4 [0.08519]	−7.2 ± 1.6 [0.1476]	−10.5 ± 1.5 **[0.0105]**	−8.5 ± 1.4 **[0.0034]**	−11.2 ± 0.9 **[0.0001]**	−16.8 ± 1.5 **[<0.0001]**
Cerebellum	−4.1 ± 2.8 [0.5629]	−9.5 ± 2.1 **[0.0145]**	−10.6 ± 1.4 **[0.0029]**	−4.9 ± 2.0 [0.3783]	−5.6 ± 3.1 [0.2713]	−7.0 ± 0.9 [0.0795]
Corpus Callosum	−9.1 ± 1.7 [0.0606]	−9.5 ± 2.2 **[0.0210]**	−12.6 ± 2.0 **[0.0012]**	−8.8 ± 1.3 [0.0776]	−10.5 ± 2.5 **[0.0339]**	−15.2 ± 1.3 **[0.0004]**
Ventricular System	−12.8 ± 2.7 **[0.0024]**	−8.6 ± 2.4 **[0.0419]**	−11.8 ± 1.7 **[0.0023]**	−13.3 ± 4.1 **[0.0283]**	−15.8 ± 5.1 **[0.0073]**	−11.5 ± 2.2 **[0.0335]**

Two-way repeated measures ANOVA (or Mixed model), Sidak post-hoc, was used for statistical analysis to compare male WT (n = 5) and KO (n = 7) and female WT (n = 6) and HET (n = 6). Animals whose fitting in the segmentation was not optimal were excluded from the analysis (n = 1 KO P20; n = 1 HET P90).

KO mouse males and HET females. Similarly, both striatum and pallidum appeared to mainly contribute to the early and advancing reduction of basal ganglia (Table 1), while thalamus and hypothalamus concurred to interbrain volume decrease. Detailing the hindbrain, we revealed a significant defect only in the pons of symptomatic KO mice, while both medulla and pons were significantly smaller in HET brains at all ages. Eventually, and in accordance with its total volume, cerebellar sub-regions revealed significant defects only in symptomatic *Mecp2* null animals.

To reveal whether specific areas impact more on the overall brain volume defect, we measured the volume of a specific region with respect to the whole brain size, therefore obtaining the relative volume. Initially we focused on major brain regions, depicted in Fig. 2A (from Brain Atlas). The analysis in *Mecp2* deficient brains revealed very few significant defects suggesting that the overall volume reduction of the RTT mouse brain is caused by a generalized decrement of most areas. We only observed a significant or barely significant difference in the hippocampus of both genders of symptomatic mice (Fig. 2C) and in the hindbrain of aged HET females (Fig. 2E). Further, symptomatic P200 HET females exhibited a trend toward an increment of the cerebellar relative volume (Fig. 2I).

Eventually, to understand which structures contribute more to the growth stagnation of the HET brain (Fig. 1C), we estimated in both genders the volume changes of analyzed brain regions with respect to the first time point of observation; most relevant results are shown in Figs.3 and 4. The KO brain confirmed that several brain areas (Fig. 3A-E left panels) had a delayed but not arrested growth, that became significantly defective at the latest time point. As a major exception, the hypothalamus did not exhibit any growth over time and growth stagnation was confirmed in the same heterozygous district (Fig. 3F).

Unexpectedly, the HET brain revealed that from P90 to P200 the growth of cerebral cortex and hippocampus exhibited a slight reversal of the curve slope, suggesting the presence of a local progressive atrophy (Fig. 3A,B right panels). By analyzing the cortical and hippocampal subregions' growth trajectory (Fig. 4), we confirmed in females an evident shrinkage at P200, with the exception for CA2; further, CA1 and dentate gyrus appeared particularly affected already at P90 (Fig. 4E,H lower panels). As expected, in the KO brain none of the analyzed regions lost volume over time (Fig. 4A-H upper panels).

2.3. The knock-in Mecp2 Y120D brain shares most of the neuroanatomical features with the knock-out model

The same experimental design was applied to a knock-in mouse model of *Mecp2* to estimate the contribution of the genetic background to the observed neuroanatomical alterations. We used the *Mecp2* Y120D mouse line, which harbors a pathogenic missense mutation that impairs, but not abolishes, Mecp2 affinity for chromatin (Gandaglia et al., 2019). This *Mecp2* mutant line is characterized by a slightly less severe condition compared to the full KO line (Gandaglia et al., 2019). By scoring mouse symptoms we confirmed that the ages of P20 for hemizygous KI males and of P60 for heterozygous females corresponded to apparently asymptomatic periods, P30 and P90 to mild symptomatic stages and P40 and P200 to fully symptomatic ages (Fig. 5A). Longitudinal analyses of total brain volume confirmed that both genders of the KI line suffered from a reduction in total cerebral size whose timing and entity highly overlapped with those observed in the KO line (see Fig. 5B and 1B for comparison). We thus analyzed the progression of defects in the same regions studied in the KO line. As shown in Table 3, most brain areas were considerably smaller in both genders at symptomatic ages, therefore mimicking the null situation. In detail, cerebral cortex, hippocampal area, basal ganglia, midbrain and corpus callosum appeared particularly affected in both genders, with the KI cerebral cortex exhibiting a greater defect with respect to the KO one. In contrast to the null line, the KI cerebellum did not show any volumetric defect in males, while a significant reduction in P200 Y120D heterozygous mice was observed. Eventually, hindbrain and ventricular system were less affected respectively in the *Mecp2* Y120D females and males in comparison to the null line.

Zooming to sub-regions of main areas (Table 4), we confirmed a strong involvement of the KI cerebral cortex and associated regions. In particular, and diversely from the KO line, prefrontal cortex and visual cortex were particularly compromised, while entorhinal cortex appeared less affected. As major difference, we also observed that *Mecp2* Y120D heterozygous medulla was preserved at all ages, while it was always defective in HET females.

As for the KO line, analysis of relative volume (Fig. 6) confirmed the presence of few significant impairments indicating that cerebral volumetric decrease mainly relies on a defective volume of most areas. Further, we confirmed the involvement of cerebral cortex in both genders and hippocampus only in males. Eventually, to highlight the

Table 2
Regional cerebral volume difference (%) of KO and HET compared to WT littermates.

Anatomical Region	Males %difference to WT (Mean ± SEM) [p value]			Females %difference to WT (Mean ± SEM) [p value]		
	P20	P30	P40	P60	P90	P200
Cerebral cortex						
Prefrontal cortex	−6.4 ± 2.9 [0.6433]	−8.6 ± 2.6 [0.2388]	−8.3 ± 2.8 [0.2797]	−7.2 ± 2.1 [0.1665]	−9.8 ± 2.7 **[0.0495]**	−13.3 ± 2.1 **[0.0039]**
Entorhinal cortex	−7.8 ± 2.1 [0.2351]	−11.5 ± 2.5 **[0.0232]**	−14.5 ± 3.0 **[0.0016]**	−11.8 ± 2.0 **[0.0090]**	−13.8 ± 2.6 **[0.0010]**	−15.7 ± 2.3 **[0.0002]**
Somatomotor cortex	−5.0 ± 1.7 [0.6746]	−9.8 ± 2.4 **[0.0167]**	−9.6 ± 1.9 **[0.0139]**	−4.8 ± 1.4 [0.2359]	−6.0 ± 2.1 [0.1392]	−11.4 ± 1.7 **[0.0006]**
Somatosensory cortex	−5.3 ± 1.7 [0.3798]	−11.1 ± 2.1 **[0.0017]**	−12.0 ± 1.6 **[0.0004]**	−5.1 ± 1.3 [0.1352]	−7.0 ± 1.7 **[0.0178]**	−11.8 ± 1.4 **[0.0001]**
Visual cortex	−2.7 ± 1.8 [0.7819]	−7.9 ± 2.1 [0.0501]	−13.0 ± 1.9 **[0.0003]**	−5.7 ± 1.9 [0.2896]	−8.9 ± 1.9 [0.1113]	−13.9 ± 3.1 **[0.0008]**
Olfactory areas	−3.0 ± 2.2 [0.8988]	−4.4 ± 4.1 [0.6733]	−4.6 ± 1.7 [0.5885]	−1.9 ± 0.5 [0.8347]	−3.9 ± 1.2 [0.3222]	−8.2 ± 1.4 **[0.0045]**
Hippocampal formation						
CA1	−10.6 ± 1.3 **[0.0036]**	−12.1 ± 2.3 **[0.0003]**	−11.9 ± 2.0 **[0.0003]**	−8.1 ± 2.0 [0.1677]	−15.4 ± 1.3 **[0.0022]**	−20.1 ± 1.0 **[<0.0001]**
CA2	4 ± 5.7 [0.9847]	−14.9 ± 5 [0.3216]	−23.09 ± 3 **[0.0244]**	−18.9 ± 7.7 [0.1333]	−5.2 ± 7.4 [0.9316]	−8.7 ± 3.7 [0.6674]
CA3	−8.9 ± 3.1 [0.2035]	−13.3 ± 1.9 **[0.0123]**	−15.8 ± 2.8 **[0.0016]**	−11.8 ± 2.1 **[0.0079]**	−15.4 ± 0.6 **[0.0009]**	−22.3 ± 2.0 **[<0.0001]**
Dentate gyrus	−13.2 ± 2.4 **[0.0038]**	−9.9 ± 1.8 **[0.0175]**	−9.7 ± 2.6 **[0.0210]**	−5.9 ± 1.7 [0.5726]	−18.0 ± 1.1 **[0.0025]**	−22.8 ± 1.4 **[<0.0001]**
Basal Ganglia						
Striatum	−6.3 ± 0.6 **[0.0234]**	−7.8 ± 1.4 **[0.0014]**	−11.1 ± 0.8 **[<0.0001]**	−8.4 ± 0.5 **[0.0023]**	−9.5 ± 1.3 **[0.0009]**	−15.0 ± 0.9 **[<0.0001]**
Pallidum	−2.5 ± 2.0 [0.7518]	−9.4 ± 1.4 **[0.0019]**	−12.9 ± 1.1 **[<0.0001]**	−8.1 ± 1.0 **[0.0028]**	−10.1 ± 1.8 **[0.0002]**	−10.6 ± 1.4 **[<0.0001]**
Interbrain						
Thalamus	−7.4 ± 1.8 **[0.0074]**	−6.7 ± 1.2 **[0.0073]**	−7.4 ± 1.4 **[0.0017]**	−8.1 ± 0.9 **[0.0022]**	−9.6 ± 1.6 **[0.0004]**	−13.7 ± 0.8 **[<0.0001]**
Hyphothalamus	−4.3 ± 2.5 [0.2955]	−13.1 ± 0.8 **[<0.0001]**	−12.4 ± 0.7 **[<0.0001]**	−7.3 ± 0.6 **[0.0103]**	−12.7 ± 1.0 **[<0.0001]**	−14.7 ± 1.7 **[<0.0001]**
Hindbrain						
Pons	−6.4 ± 2.6 [0.3142]	−11.4 ± 1.2 **[0.0073]**	−14.0 ± 1.4 **[0.0006]**	−9.8 ± 1.6 **[0.0156]**	−14.1 ± 1.4 **[0.0005]**	−18.8 ± 1.4 **[<0.0001]**
Medulla	−1.1 ± 2.6 [0.9924]	−4.9 ± 2.3 [0.5675]	−8.6 ± 2.1 [0.0854]	−7.7 ± 2.0 **[0.0169]**	−9.8 ± 1.1 **[0.0020]**	−15.7 ± 1.7 **[<0.0001]**
Cerebellum						
Cerebellar Cortex	−4.3 ± 2.9 [0.5434]	−9.6 ± 2.1 **[0.0135]**	−10.7 ± 1.4 **[0.0029]**	−4.7 ± 2.1 [0.3965]	−5.7 ± 3.1 [0.2496]	−7.1 ± 0.9 [0.0737]
Vermal Region	−4.4 ± 3.4 [0.4828]	−7.8 ± 2.2 [0.0660]	−12.8 ± 1.3 **[0.0005]**	−5.7 ± 2.9 [0.4119]	−5.3 ± 3.1 [0.5286]	−8.3 ± 1.0 [0.0957]

Two-way repeated measures ANOVA (or Mixed model), Sidak post-hoc, was used for statistical analysis to compare male WT ($n = 5$) and KO ($n = 7$) and female WT ($n = 6$) and HET (n = 6). Animals whose fitting in the segmentation was not optimal were excluded from the analysis ($n = 1$ KO P20; n = 1 HET P90).

possible occurrence of atrophic processes, we investigated how the most affected regions change their volume with respect to the first time point of analysis. Unfortunately, due to technical issues, two females from the growth trajectory analysis had to be excluded, thus impeding to parallel male results with female ones. Obtained results confirmed the absence of atrophy when main brain areas (such as cortex and hippocampus) were considered (Fig. 7A,D), while the analysis of the sub-areas disclosed the presence of an atrophic phenotype in specific structures, as visual cortex, CA1 and dentate gyrus. The growth stagnation described for the *Mecp2* KO and HET hypothalamus was confirmed in the KI male brain (Fig. 7G).

2.4. *Defective protein synthesis might participate to the observed regional atrophy in HET brains*

Our data highlighted the presence of a regional brain shrinkage, particularly in aged HET female brains. We thus found it relevant to investigate which factors might contribute to this phenotype. To this purpose, based on Fig. 4 results, we focused on P200 somatosensory cortex and CA1 of *Mecp2* HET mice. Nissl staining confirmed in both cerebral regions the expected increase in cell density, that in RTT is usually associated with a decrease in dendritic arborization and a reduction in neuronal soma size (Belichenko et al., 2009). On the contrary, this defect was not evident in young HET females (Fig. 8A).

The RTT mouse brain is characterized by reduced protein synthesis, a phenotype well represented by a decrement of ribosomal protein S6 phosphorylation but not of total S6 (Ricciardi et al., 2011). Since this defect might contribute to the observed atrophy, we used immunofluorescence to quantify phospho-rpS6 in pre-symptomatic (P30) and fully symptomatic HET brains (P200). Importantly, we confirmed the presence of defective phosphorylation in *Mecp2* HET somatosensory cortex and CA1 at P200, whilst no phenotype was observed at P30 (Fig. 8B-I).

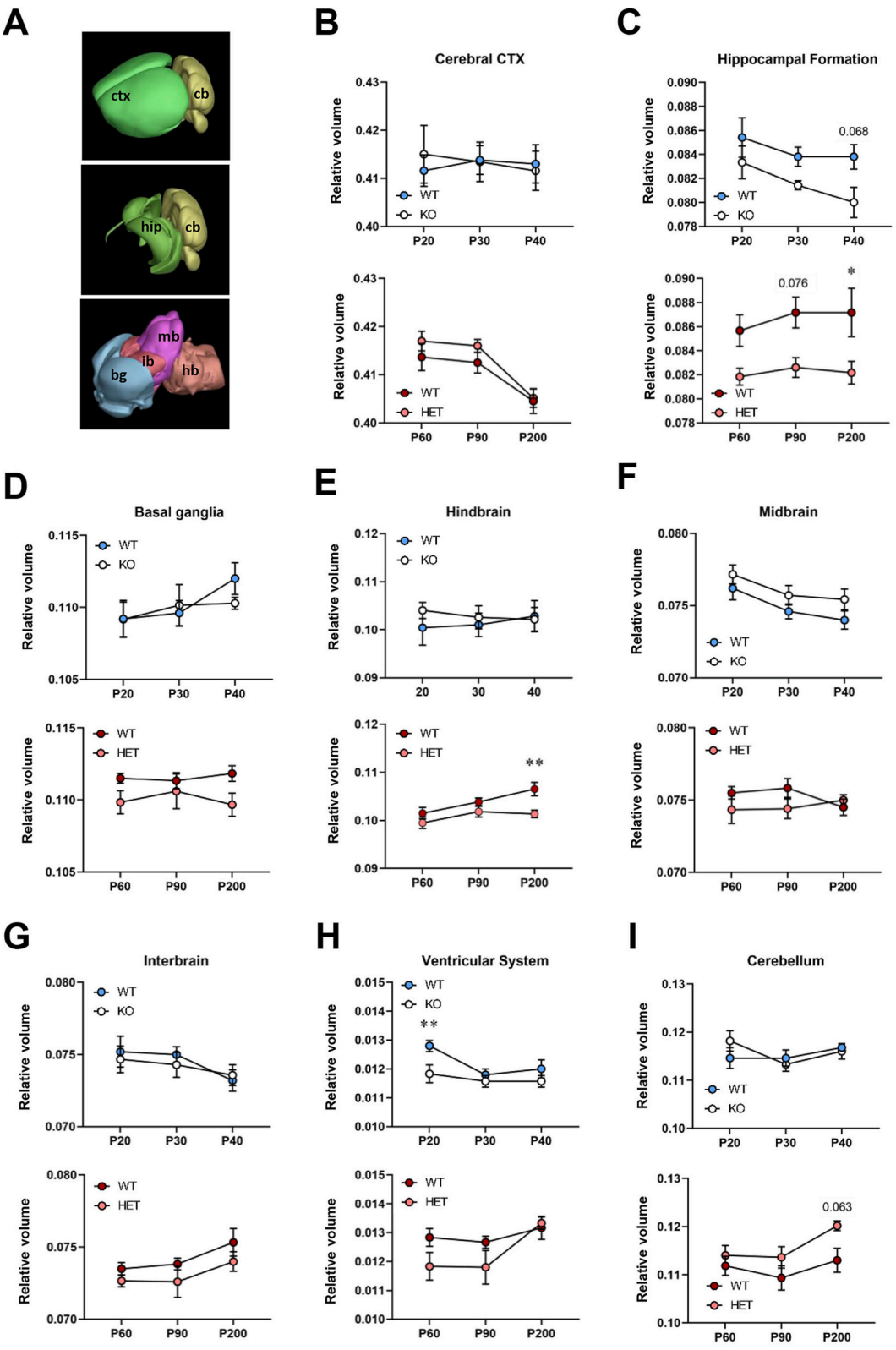

Fig. 2. (A) The main brain regions analyzed are indicated in the cartoon and the table (obtained from Mouse Brain Atlas; bg: basal ganglia; cb: cerebellum; ctx: cerebral cortex; hb: hindbrain; hip: hippocampus; ib.: interbrain; mb: midbrain). (B—I) Graphs show the relative volume of the cerebral cortex (B), hippocampal formation (C), basal ganglia (D), hindbrain (E), midbrain (F), interbrain (G), ventricular system (H) and cerebellum (I) in both males (upper panel; WT, $n = 5$; *Mecp2* KO, n = 7) and females (lower panel; WT, $n = 6$; HET, n = 6) from *Mecp2* null line. The hippocampal formation appears affected in mutant animals of both genders, while defects in hindbrain and cerebellum were noticed only in aged mutant females. Animals whose fitting in the segmentation was not optimal were excluded from the analysis. Each mutant mouse was evaluated in comparison to its WT littermates by Two-way repeated measures ANOVA or Mixed-Model Analysis, followed by Sidak post-hoc; $*p < 0.05$; $**p < 0.01$.

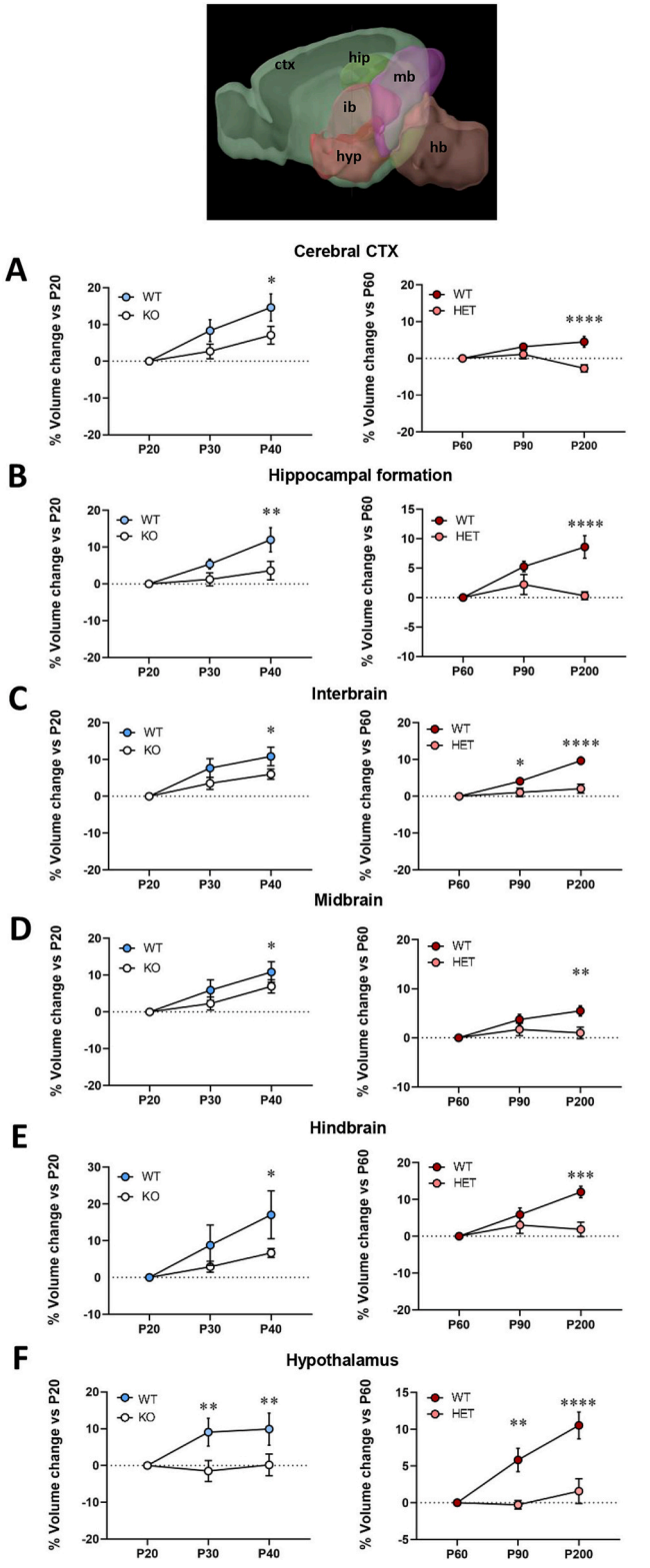

Fig. 3. Graphs depict the developmental trajectory of different brain regions in comparison to the first time point of analysis in *Mecp2* null animals of both genders (males, left panel; WT, $n = 5$; KO, n = 7; females, right panel; WT, $n = 6$; HET, n = 6). Each mutant mouse was evaluated in comparison to its WT littermates by Two-way repeated measures ANOVA or Mixed-Model Analysis, followed by Fisher's LSD post-hoc; *$p < 0.05$; **$p < 0.01$; ***$p < 0.001$; ****$p < 0.0001$. The cartoon highlights the analyzed brain regions (obtained from Mouse Brain Atlas; ctx: cerebral cortex; hb: hindbrain; hip: hippocampus; hyp: hypothalamus; ib.: interbrain; mb: midbrain).

2.5. Longitudinal MRS analyses do not reveal evident metabolic biomarkers

Together with morphological analysis by MRI, cerebral metabolism was assessed by MRS in all animals. We selected the highly affected hippocampus of *Mecp2* KO males and HET females and included the cerebellum to investigate whether metabolic alterations might correlate with volumetric defects. The following cerebral metabolites were quantified: creatine with phosphocreatine (Cr + PCr) or PCr alone, gamma-aminobutyric acid (GABA), glutamine (Gln), glutamate (Glu) and the Glu/Gln ratio, glutathione, glycerophosphorylcholine with phosphatidylcholine (GPC + PCh), inositol, *N*-acetyl aspartate (NAA) and NAA with *N*-acetyl-aspartyl-glutamate (NAA + NAAG) and taurine (Table 5).

The analysis performed in the hippocampus of KO symptomatic mice revealed the largest number of significant alterations in metabolites' concentration, expressed in mM. In particular, GABA which is the major inhibitory neurotransmitter in the central nervous system, showed a significant decrease in KO male compared to their WT littermates at P40 (WT: 2.47 ± 0.11; KO 2.06 ± 0.15; −17% compared to WT, $p < 0.05$), possibly suggesting a reduction in synaptic function (Asaka et al., 2006). On the contrary, glutamine levels were significantly higher in KO hippocampi, varying from +26% at P20 (WT: 2.70 ± 0.27; KO 3.45 ± 0.27; $p = 0.0408$) and P30 (WT: 3.33 ± 0.13; KO 4.19 ± 0.15; $p = 0.0115$) to +30% at P40 (WT: 3.05 ± 0.43; KO 3.97 ± 0.09; $p = 0.0107$), therefore leading to a decrement of almost 30% in the Glu/Gln ratio (WT: 3.33 ± 0.50; KO 2.26 ± 0.12; $p = 0.0080$). A significant defect in PCr (up to −35%), which serves in brain ATP homeostasis, was also observed at P20 (WT: 7.26 ± 0.44; KO 4.73 ± 0.34; $p = 0.0006$) and P40 (WT: 6.96 ± 0.52; KO 4.82 ± 0.29; $p = 0.0089$). Of note, at P40, a defect in the antioxidant glutathione was also found (WT: 2.62 ± 0.21; KO 2.07 ± 0.15; −21% compared to WT; $p = 0.0488$).

No consistent alteration was identified in HET mice; we believe that the higher phenotypic variability caused by random X chromosome inactivation might justify this result.

The same study applied to the *Mecp2* null cerebellum confirmed an unbalanced Glu/Gln ratio. No additional defect was detected apart from a deficiency in inositol and NAA in pre-symptomatic mice, therefore confirming that the metabolic disequilibrium in the RTT brain is region specific (Supplementary Table 1). As for KO mice, no significant result was obtained in the HET cerebellum.

3. Discussion

Several years have passed since the breaking through discovery that Rett syndrome does not represent an irreversible condition (Ip et al., 2018). Although this study has dramatically accelerated pre-clinical and clinical studies aimed at finding possible treatments, no cure is still available for the treatment of RTT. The lack of a full comprehension of the pathogenic mechanisms contributing to RTT symptoms and of quantitative and translational biomarkers exploitable to test drug efficacy might have contributed to this delay.

Neuroimaging techniques, such as MRI and MRS, had already been successfully used in RTT patients and mouse models of *Mecp2* to investigate the consequences of MeCP2 deficiency. However, comprehensive longitudinal studies of neuroimaging and MRS aimed at identifying how the disease progresses with time are needed to further determine which cerebral regions are predominantly affected, and whether results are consistent between genders and/or different *Mecp2* mouse lines. This gap of knowledge promoted our studies in which we took advantage of the largely used *Mecp2*$^{tm1.1Bird}$ null line and a *Mecp2* Y120D knock-in line that reproduces a human pathogenic mutation (Gandaglia et al., 2019; Guy et al., 2001). Previous backcrossing of the two lines in the CD1 outbred genetic background provided us with larger litters and more robust animals therefore speeding up the study and facilitating the analyses under anaesthesia (Cobolli Gigli et al., 2016).

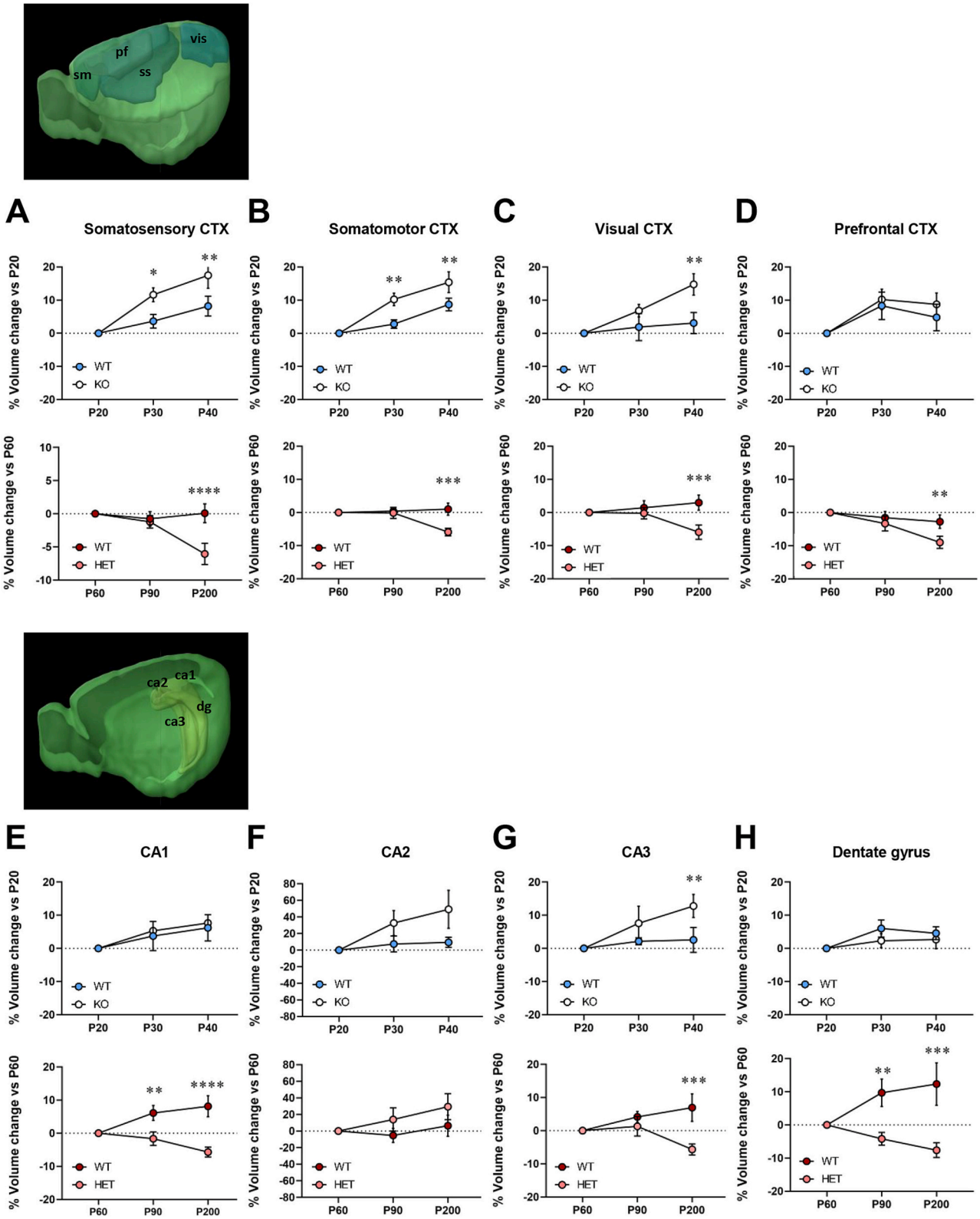

Fig. 4. Graphs show the developmental trajectory in *Mecp2* null animals of different portions of the cerebral cortex (A-D) and of the hippocampal formation (*E*-H) in comparison to the first time point of analysis. Mutant males (WT, n = 5; KO, n = 7) and females (WT, n = 6; HET, n = 6) are compared to WT littermates. Animals whose fitting in the segmentation was not optimal were excluded from the analysis. Each mutant mouse was evaluated in comparison to its WT littermates by Two-way repeated measures ANOVA or Mixed-Model Analysis, followed by Fisher's LSD post-hoc; *$p < 0.05$; **$p < 0.01$; ***$p < 0.001$; ****$p < 0.0001$. Cartoons represent the analyzed brain sub-regions and are obtained from Mouse Brain Atlas. Upper cartoon, pf: prefrontal cortex; sm: somatomotor cortex; ss: somatosensory cortex; vis: visual cortex; lower cartoon, ca1,2,3: cornu ammonis; dg: dentate gyrus.

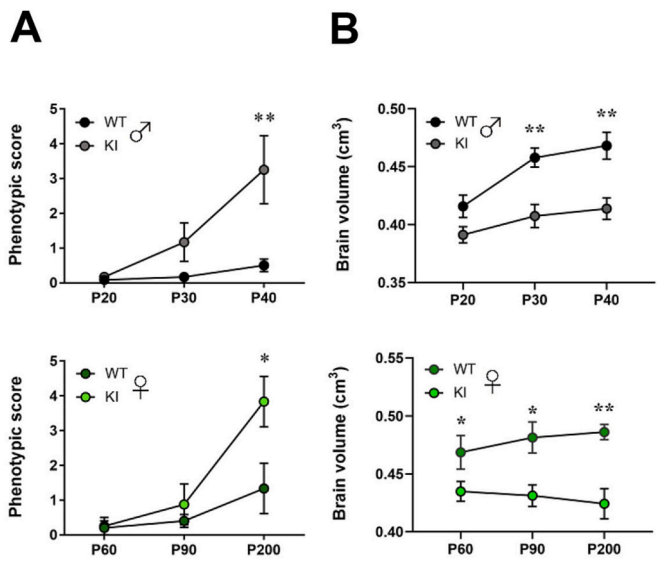

Fig. 5. (A) Graphs display the evolution of the phenotypic score, cumulated for general condition, mobility, hind limb clasping, gait and tremor in male (upper panel) and female (lower panel) mice from the *Mecp2* Y120D line. (B) *In vivo* longitudinal MRI shows a significant reduction in the total brain volume (cm^3) of *Mecp2* Y120D animals of both genders. Male mice (upper panel) show a significant defect since P30, female brains (lower panel) are smaller than WT counterparts at any time point of analysis. Male mice: WT, n = 5; KI, n = 6. Female mice WT, n = 6; HET, n = 6. Animals whose fitting in the segmentation was not optimal were excluded from the analysis. Each mutant mouse was evaluated in comparison to its WT littermates by Two-way repeated measures ANOVA or Mixed-Model Analysis, followed by Sidak post-hoc; *p < 0.05; **p < 0.01.

Time points of analyses corresponded to a pre-symptomatic time point, a barely-symptomatic age and a fully-symptomatic stage. Of relevance, these time points in heterozygous females are delayed with respect to the hemizygous male mice. To obtain unbiased results we used an advanced automatic atlas-based segmentation tool, widely used for both clinical and preclinical data, that permitted a detailed whole-brain anatomical analysis (Koch et al., 2019).

Most relevant features identified in the *Mecp2* deficient brains have been summarized in Table 6; for convenience, only data derived from pre-symptomatic and fully symptomatic time points are reported. In particular, and in good accordance with clinical data obtained from RTT patients and previous neuroimaging studies of mouse models of *Mecp2,* our data confirmed that the most robust neuropathological change consists in an overall reduction of brain volume, while MRS study established the expected alteration of neurotransmitters.

Importantly, reduction of brain volume of some cerebral regions anticipates the onset of overt symptoms and correlates with disease progression in both genders and mutant lines. Indeed, at P60, apparently asymptomatic mutant females exhibit a significant reduction of whole brain volume that, instead, is still not present at P20, in the brain of asymptomatic hemizygous male mice, although specific regions are already affected. Further, in hemizygous *Mecp2* deficient mice, total brain growth is slower than normal, whereas in older heterozygous females, growth stagnation is observed. According to its role in brain development and maintenance of the mature state (Ip et al., 2018), we believe that *Mecp2* deficiency generally delays brain growth, eventually leading to stagnation and deterioration, a phenotype that can be more easily appreciated in animals with long lifespan. This hypothesis might be confirmed analyzing hemizygous *Mecp2*$^{308/y}$ mice (Shahbazian et al., 2002).

In agreement, analysis of major brain areas confirmed a general and progressive volumetric decrement in all *Mecp2* deficient mice with prominent defects of cerebrum and brainstem and minor involvement of cerebellum. Interestingly, a temporary defect in the size of the mouse *Mecp2* null cerebellum had already been reported (Stearns et al., 2007; Ward et al., 2008), and recent analyses on RTT patients might suggest a similar trend. Indeed, while voxel-based morphological measurements in young RTT patients (mean age: 5.2 years old) identified a significant loss of the cerebellar volume, a different study performed in adult patients reported that cerebral hemispheres have a more evident size defect with respect to the cerebellum (Shiohama et al., 2019; Mahmood et al., 2010). These results might suggest that the well-known motor defects of RTT mice might be caused by defective basal ganglia and motor cortex, which in our study appeared more affected. In possible good accordance, it has been recently published that conditional inactivation of *Mecp2* from the cerebellum only causes delay in motor learning, that however can be overcome by training (Achilly et al., 2021).

The volumetric analysis permitted also to highlight a strong and

Table 3
Volume difference (%) of *Mecp2 Y120D* mutant male and female mice compared to WT littermates.

Anatomical Region	Males %difference to WT (Mean ± SEM) [p value]			Females %difference to WT (Mean ± SEM) [p value]		
	P20	P30	P40	P60	P90	P200
Cerebral cortex	−8.4 ± 2.5 [0.0713]	−12.5 ± 2.2 **[0.0018]**	−13.6 ± 1.9 **[0.0005]**	−8.1 ± 2.3 **[0.0176]**	−11.6 ± 2.3 **[0.0104]**	−15.2 ± 3.0 **[0.0017]**
Hippocampal formation	−9.0 ± 2.8 [0.0592]	−12.5 ± 2.9 **[0.0031]**	−15.2 ± 1.8 **[0.0003]**	−7.8 ± 1.1 **[0.0080]**	−12.6 ± 2.7 **[0.0019]**	−15.3 ± 2.1 **[0.0013]**
Basal ganglia	−6.9 ± 2.9 [0.1442]	−9.3 ± 2.2 **[0.0151]**	−8.7 ± 2.0 **[0.0208]**	−5.1 ± 1.8 [0.1291]	−9.0 ± 2.0 **[0.0216]**	−13.2 ± 2.7 **[0.0009]**
Interbrain	−5.7 ± 3.2 [0.3029]	−11.1 ± 2.0 **[0.0058]**	−10.6 ± 2.2 **[0.0071]**	−8.1 ± 1.8 **[0.0107]**	−9.6 ± 2.0 **[0.0106]**	−13.1 ± 1.9 **[0.0006]**
Midbrain	−10.1 ± 3.2 [0.0596]	−12.4 ± 1.8 **[0.0081]**	−12.5 ± 2.7 **[0.0056]**	−6.0 ± 2.2 [0.1132]	−9.8 ± 2.0 **[0.0206]**	−11.7 ± 2.9 **[0.0112]**
Hindbrain	−5.2 ± 2.8 [0.4409]	−7.3 ± 2.6 [0.1148]	−8.6 ± 2.4 **[0.0481]**	−9.6 ± 2.3 [0.0774]	−10.0 ± 1.8 [0.0593]	−5.2 ± 3.2 [0.6951]
Cerebellum	−11.5 ± 5.5 [0.1046]	−8.5 ± 3.0 [0.2369]	−10.2 ± 1.9 [0.0929]	−4.1 ± 1.9 [0.2761]	−8.8 ± 1.9 [0.0595]	−10.2 ± 3.6 **[0.0172]**
Corpus Callosum	−9.4 ± 1.8 **[0.0363]**	−15.2 ± 2.8 **[0.0003]**	−17.1 ± 2.8 [<**0.0001**]	−11.1 ± 2.5 **[0.0177]**	−8.6 ± 3.0 [0.1296]	−21.2 ± 2.9 **[0.0011]**
Ventricular System	−11.0 ± 3.3 [0.1110]	−11.2 ± 2.2 [0.0742]	−6.7 ± 3.6 [0.4361]	−5.5 ± 4.2 [0.5674]	−10.9 ± 1.9 **[0.0291]**	−19.8 ± 3.4 **[0.0005]**

Two-way repeated measures ANOVA (or Mixed model), Sidak post-hoc, was used for statistical analysis to compare male WT (n = 5) and KI (n = 6) and female WT (n = 6) and HET (n = 6). Animals whose fitting in the segmentation was not optimal were excluded from the analysis (n = 1 female WT P200; n = 1 HET P200).

Table 4
Regional cerebral volume difference (%) of KI and HET compared to WT littermates.

Anatomical Region	Males %difference to WT (Mean ± SEM) [p value]			Females %difference to WT (Mean ± SEM) [p value]		
	P20	P30	P40	P60	P90	P200
Cerebral cortex						
Prefrontal cortex	−12.9 ± 3.6 [0.0591]	−14.9 ± 3.7 **[0.0096]**	−17.4 ± 2.2 **[0.0027]**	−7.6 ± 2.5 [0.2986]	−16.0 ± 3.9 **[0.0291]**	−27.0 ± 4.6 **[0.0023]**
Entorhinal cortex	−6.3 ± 2.6 [0.3393]	−9.5 ± 2.8 [0.0585]	−13.9 ± 2.0 **[0.0024]**	−7.0 ± 2.0 [0.0607]	−11.8 ± 2.9 **[0.0233]**	−13.8 ± 2.2 **[0.0194]**
Somatomotor cortex	−12.2 ± 2.9 **[0.0202]**	−16.9 ± 2.2 **[0.0002]**	−15.5 ± 2.2 **[0.0006]**	−9.0 ± 3.1 [0.0509]	−12.5 ± 1.8 **[0.0111]**	−18.5 ± 3.6 **[0.0005]**
Somatosensory cortex	−10.2 ± 2.7 [0.0920]	−15.5 ± 2.6 **[0.0018]**	−16.1 ± 2.7 **[0.0014]**	−9.9 ± 3.9 **[0.0241]**	−11.2 ± 2.4 **[0.0345]**	−19.5 ± 3.2 **[0.0005]**
Visual cortex	−7.9 ± 2.2 [0.1554]	−12.2 ± 2.7 **[0.0071]**	−18.7 ± 1.4 [<**0.0001**]	−9.4 ± 2.0 **[0.0089]**	−11.7 ± 2.6 **[0.0102]**	−18.0 ± 1.5 **[0.0004]**
Olfactory areas	−5.2 ± 3.1 [0.4884]	−7.5 ± 2.1 [0.1315]	−8.5 ± 2.3 [0.0536]	−7.9 ± 2.3 [0.0504]	−10.9 ± 2.4 **[0.0331]**	−7.5 ± 3.8 [0.2446]
Hippocampal formation						
CA1	−11.0 ± 2.5 **[0.0137]**	−11.2 ± 2.7 **[0.0081]**	−15.8 ± 1.9 **[0.0002]**	−8.5 ± 2.7 **[0.0200]**	−12.9 ± 3.2 **[0.0061]**	−19.6 ± 3.3 **[0.0010]**
CA2	−22.4 ± 4.4 [0.0905]	−27.2 ± 6.0 **[0.0303]**	5.4 ± 6.8 [0.9603]	−8.0 ± 4.3 [0.8838]	−12.2 ± 7.4 [0.6447]	−24.3 ± 13.5 [0.2754]
CA3	−10.2 ± 4.5 [0.2525]	−17.6 ± 5.5 **[0.0101]**	−18.8 ± 2.6 **[0.0061]**	−7.9 ± 3.9 [0.1919]	−17.3 ± 3.3 **[0.0021]**	−7.8 ± 3.4 [0.4715]
Dentate gyrus	−10.0 ± 2.6 **[0.0311]**	−9.6 ± 3.3 **[0.0255]**	−16.1 ± 2.0 **[0.0002]**	−8.2 ± 3.5 [0.2082]	−12.0 ± 3.1 **[0.0438]**	−14.2 ± 4.3 [0.0990]
Basal Ganglia						
Striatum	−6.5 ± 2.8 [0.1926]	−10.1 ± 2.2 **[0.0088]**	−9.1 ± 2.1 **[0.0171]**	−5.4 ± 1.6 [0.0853]	−9.2 ± 2.1 **[0.0158]**	−12.7 ± 2.8 **[0.0011]**
Pallidum	−8.6 ± 3.2 [0.0707]	−5.6 ± 2.4 [0.2851]	−7.0 ± 1.9 [0.1160]	−3.7 ± 2.9 [0.6847]	−7.6 ± 1.8 [0.1450]	−15.6 ± 3.1 **[0.0039]**
Interbrain						
Thalamus	−6.6 ± 2.9 [0.2648]	−11.1 ± 2.5 **[0.0110]**	−8.7 ± 2.4 [0.0506]	−7.9 ± 2.5 **[0.0180]**	−8.4 ± 2.3 **[0.0450]**	−14.8 ± 2.5 **[0.0008]**
Hyphothalamus	−4.7 ± 3.9 [0.5477]	−11.2 ± 2.1 **[0.0143]**	−13.0 ± 2.4 **[0.0029]**	−8.2 ± 1.0 **[0.0458]**	−11.1 ± 2.2 **[0.0050]**	−10.9 ± 2.2 **[0.0120]**
Hindbrain						
Pons	−4.4 ± 2.9 [0.6926]	−11.0 ± 3.7 **[0.0268]**	−12.1 ± 2.5 **[0.0164]**	−11.5 ± 2.9 [0.0649]	−11.6 ± 2.2 [0.0515]	−3.0 ± 2.8 [0.8165]
Medulla	−5.5 ± 4.0 [0.4643]	−5.3 ± 2.2 [0.4278]	−6.9 ± 2.5 [0.2097]	−8.6 ± 4.0 [0.2423]	−9.3 ± 1.6 [0.1407]	−6.3 ± 3.8 [0.7596]
Cerebellum						
Cerebellar Cortex	−11.6 ± 5.5 [0.1009]	−8.3 ± 3.1 [0.2501]	−10.3 ± 1.8 [0.0906]	−4.1 ± 1.9 [0.2775]	−8.7 ± 2.0 [0.0683]	−10.0 ± 3.6 **[0.0210]**
Vermal Region	−15.8 ± 7.8 [0.0635]	−8.9 ± 2.9 [0.3799]	−10.7 ± 2.3 [0.2037]	−3.2 ± 3.0 [0.6362]	−7.8 ± 1.6 [0.1695]	−11.0 ± 3.3 **[0.0421]**

Two-way repeated measures ANOVA (or Mixed model), Sidak post-hoc, was used for statistical analysis to compare male WT (n = 5) and KI (n = 6) and female WT (n = 6) and HET (n = 6). Animals whose fitting in the segmentation was not optimal were excluded from the analysis (n = 1 female WT P200; n = 1 HET P200).

consistent involvement of the hippocampus. Further, relative volume indicated a major involvement of cerebral cortex in the *Mecp2* KI mouse line compared to the null one; this result was reinforced by measuring absolute volume of principal subareas of the cerebral cortex. The major difference was identified at the prefrontal cortex level; indeed, symptomatic *Mecp2* Y120D male and female mice revealed a volumetric defect whose entity was almost twice that one observed in *Mecp2* KO mice. In possible good accordance, MRI analysis of RTT patients' cortices have led to inconsistent results. Although these disparities might have been caused by measurements occurring in different cortical subareas (Stearns et al., 2007), our data suggest that different *MECP2* mutations might diversely impact cerebral cortex, while having a more consistent effect on the hippocampus.

Recent *ex vivo* studies suggested that *Mecp2* deficiency diversely affects the two hemispheres (Akaba et al., 2022). Instructed by the publication, we compared right and left regions of symptomatic *Mecp2* null male mice (P40) without, however, obtaining any relevant difference (data not shown). These discrepancies are probably due to the analysis performed on perfused and extracted tissues while our study was performed on living mice.

Finally, our longitudinal study made it possible to follow the progression of the volumetric changes of several brain areas over time in each animal. The study performed in *Mecp2* deficient male mice, analyzed at younger age and in a shorter lifespan with respect to females, confirmed, as already mentioned, that most brain structures are characterized by a slow but progressive growth, reinforcing the well-known concept of lack of degeneration. The only noteworthy region is the hypothalamus which showed to suffer from growth stagnation from an early age, a result that was confirmed also in HET females. Interestingly, conditional deletion of *Mecp2* from the hypothalamus induced

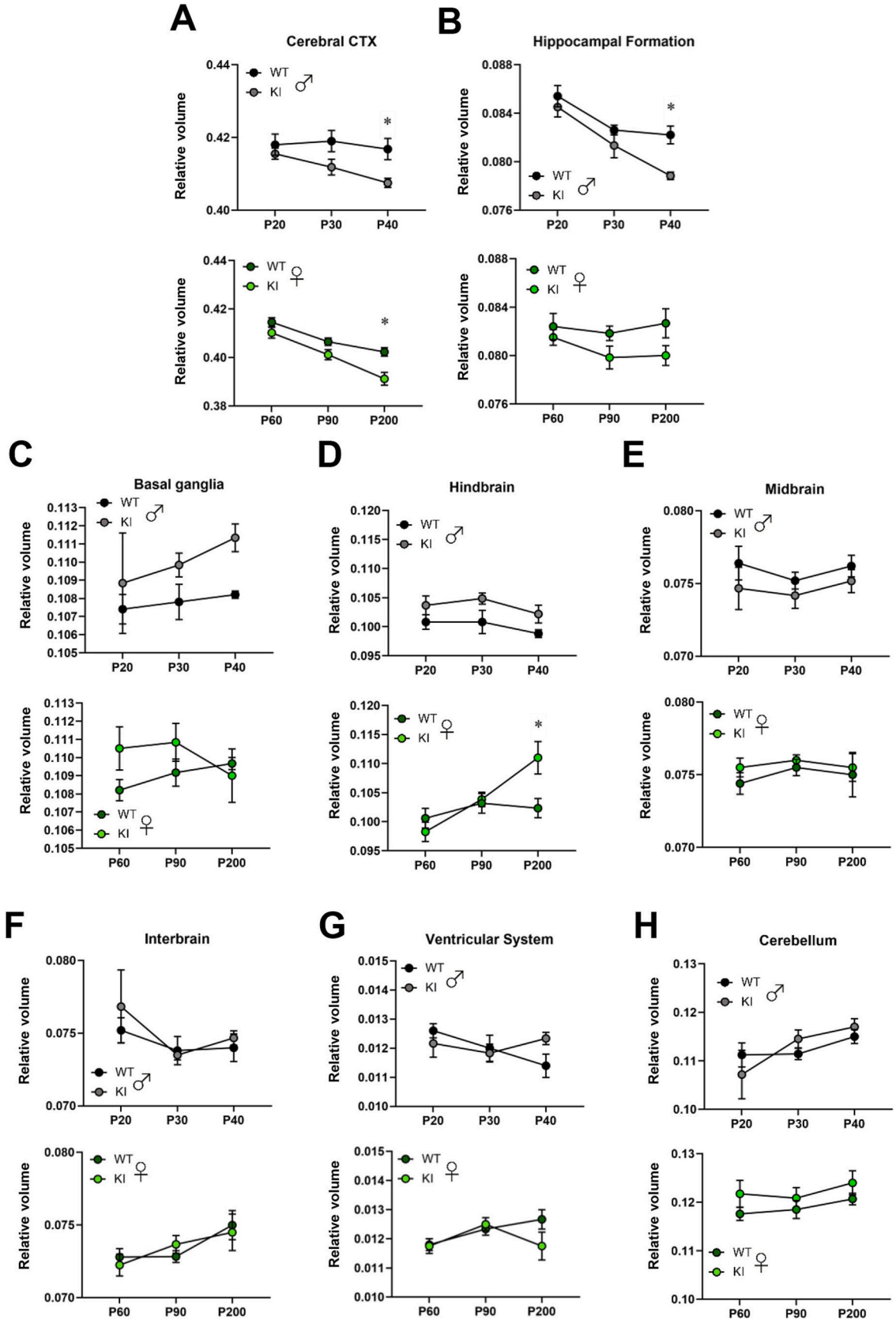

Fig. 6. (A-H) Graphs show the relative volume of the cerebral cortex (A), hippocampal formation (B), basal ganglia (C), hindbrain (D), midbrain (E), interbrain (F), ventricular system (G) and cerebellum (H) in both males (upper panel; WT, n = 5; KI, n = 6) and females (lower panel; WT, n = 6; HET, n = 6) from the *Mecp2* Y120D line. Mutant males unveil a smaller cerebral cortex and hippocampus in symptomatic animals. Mutant females show the same cerebral cortex reduction and a significant increase in the hindbrain at P200. Animals whose fitting in the segmentation was not optimal were excluded from the analysis. Each mutant mouse was evaluated in comparison to its WT littermates by Two-way repeated measures ANOVA or Mixed-Model Analysis, followed by Sidak post-hoc; *$p < 0.05$; **$p < 0.01$.

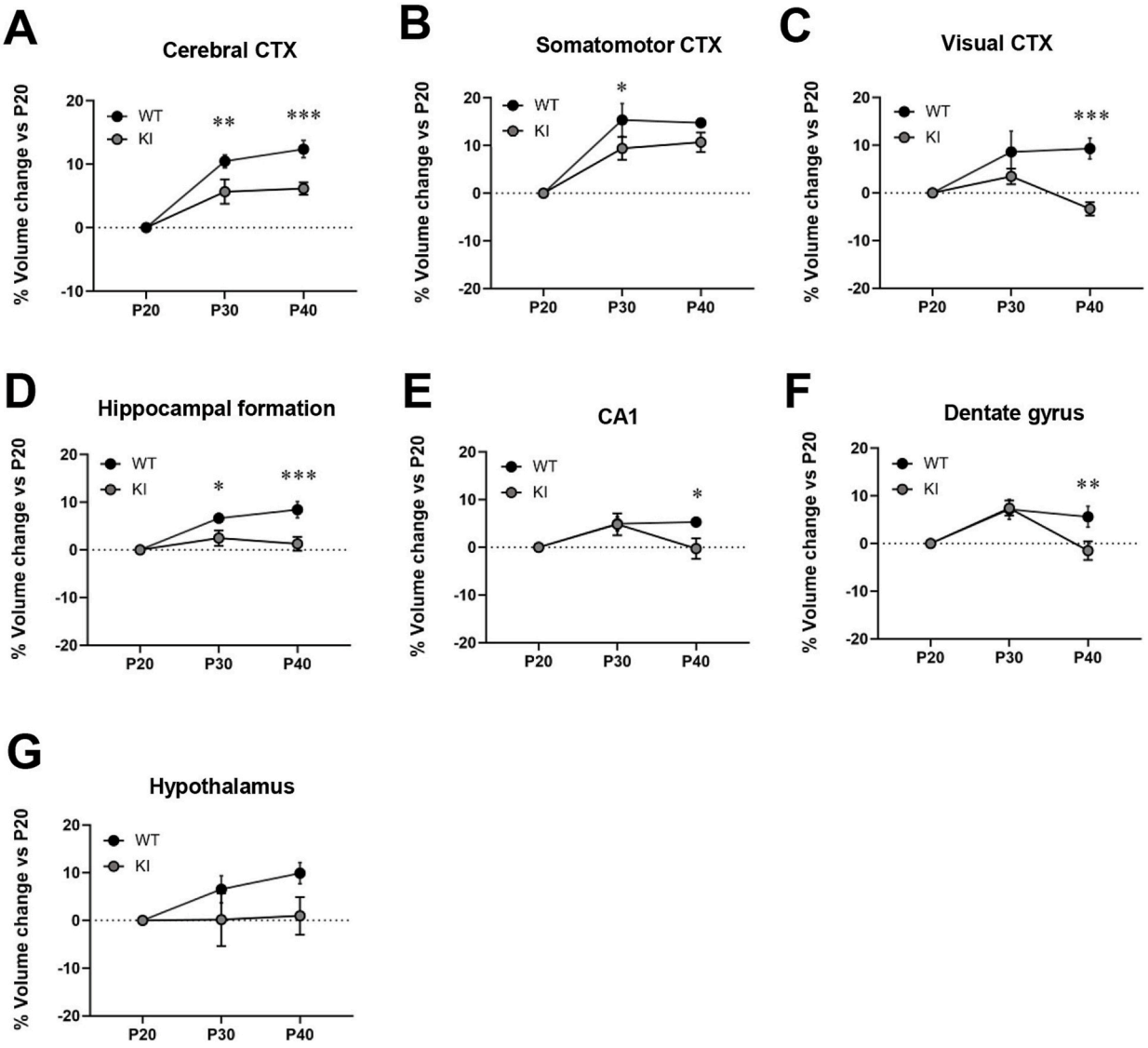

Fig. 7. Graphs unveil the developmental trajectory of cerebral cortex (A), somatomotor cortex (B), visual cortex (C), hippocampal formation (D), CA1 field (E), dentate gyrus (F) and hypothalamus of the KI male brain (WT, n = 5; KI, n = 6) in comparison to the first time point of analysis. Animals whose fitting in the segmentation was not optimal were excluded from the analysis. Each mutant mouse was evaluated in comparison to its WT littermates by Two-way repeated measures ANOVA or Mixed-Model Analysis, followed by Fisher's LSD post-hoc; *p < 0.05; **p < 0.01; ***p < 0.001; ****p < 0.0001.

aggressive, hyperphagic and obese phenotypes together with abnormal response to stress, therefore highlighting its relevant role, at least in *Mecp2* mutant mice (Fyffe et al., 2008).

The same analysis in HET females led to an unexpected result, namely the presence in most areas of the hippocampus and cortex of a loss of volume at older age (P200). However, *in vivo* MRS did not detect in the hippocampus of these HET females any alteration in NAA concentration, the neurochemical marker of neuronal integrity. As expected, cerebral atrophy does not correspond to cell death, but correlates with an increase in brain cell density and defective phosphorylation of ribosomal protein S6, associated with the rate of protein translation.

Interestingly, defects in protein synthesis represent an important aspect of memory impairment and brain aging (Kuijpers, 2022; Schimanski and Barnes, 2010); in the future, we will thus investigate whether *Mecp2* deficiency might foster brain aging in HET female mice with respect to the WT counterparts. Notably, a possible link between MeCP2 deficiency and neuron senescence has already been proposed (Squillaro et al., 2012).

4. Conclusions

Through a comprehensive *in vivo* longitudinal study of MRI and MRS performed in the brain of both genders of two mouse models of *Mecp2*, we have provided evidence that regional specific volumetric defects can anticipate overt symptoms, therefore providing a useful biomarker for the disease progression and, possibly, drug efficacy. On the contrary, MRS analysis of cerebral metabolism was limited in providing specific biomarkers at least in the studied mouse areas.

Further, MRI results from *Mecp2* deficient mouse models generally overlap with clinical observations, therefore supporting the validity of these models. Importantly, the analyses in older HET mice permitted to disclose the presence of an atrophic phenotype that has never been described before and that might be difficult to reveal in RTT patients that cannot be routinely scanned by MRI.

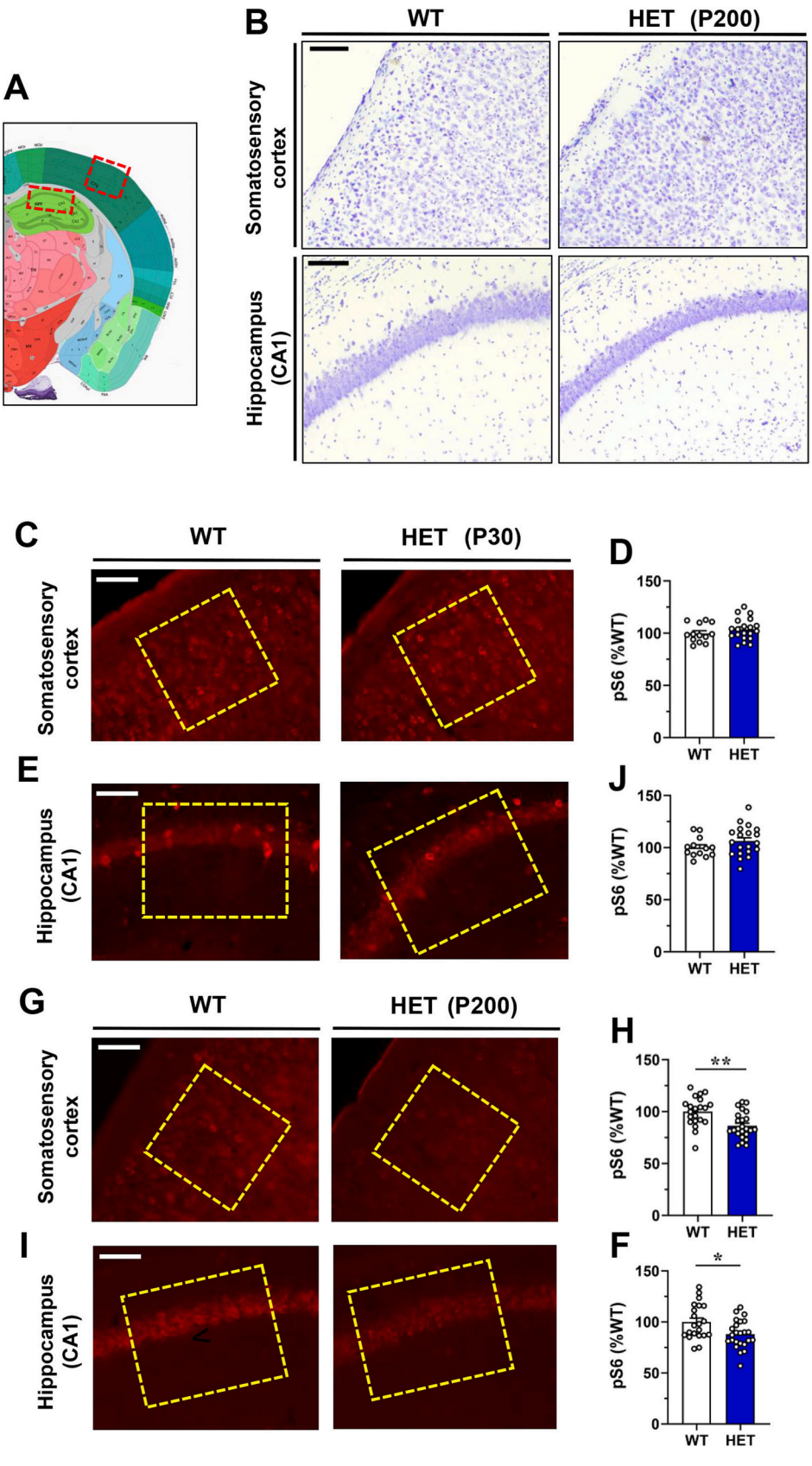

Fig. 8. (A) Representative images of Nissl staining in somatosensory cortex and hippocampal CA1 of heterozygous (HET) and female WT at P30 and P200. Scale bar: 200 μm. (B,I) Immunofluorescence analysis of phosphorylated rpS6 in the somatosensory cortex and hippocampal CA1 of HET at P30 and P200 and aged-matched female WT animals. Representative images of phospho-rpS6 staining are reported for P30 (B,D) and P200 animals. Scale bar: 100 μm. (F,H). Yellow boxes indicate the selected area for the analysis. Histograms show the integrated density of phospho-rpS6 signal, expressed as percentage of corresponding WT, in P30 (C,E) and in P200 animals (G,I). Data are reported as mean ± SEM (n = 3 WT and n = 3 HET for each time point) and analyzed by Student's t-test. *p < 0.05; **p < 0.01. (For interpretation of the references to color in this figure legend, the reader is referred to the web version of this article.)

Table 5
Metabolite concentration (mM) in the hippocampus of KO and HET mice.

	Male						Female					
	WT			KO			WT			HET		
Metabolites	P20	P30	P40	P20	P30	P40	P60	P90	P200	P60	P90	P200
Cr + PCr	7.73 ± 0.10 (5)	7.49 ± 0.08 (5)	7.94 ± 0.27 (5)	7.47 ± 0.31 (7)	7.69 ± 0.43 (7)	7.45 ± 0.34 (6)	7.86 ± 0.31 (6)	8.15 ± 0.46 (5)	7.40 ± 0.12 (6)	8.68 ± 0.32 (6) $p = 0.0615$	8.60 ± 0.43 (5)	7.92 ± 0.18 (6)
GABA	1.64 ± 0.20 (5)	2.32 ± 0.17 (5)	2.47 ± 0.11 (5)	1.77 ± 0.12 (7)	2.25 ± 0.12 (6)	**2.06 ± 0.15** (6)*	2.31 ± 0.11 (6)	2.29 ± 0.20 (5)	2.26 ± 0.24 (6)	2.30 ± 0.32 (5)	2.21 ± 0.11 (4)	2.33 ± 0.14 (6)
Glutamine (Gln)	2.70 ± 0.27 (4)	3.33 ± 0.13 (5)	3.05 ± 0.43 (5)	**3.45 ± 0.27** (5)*	**4.19 ± 0.15** (7)*	**3.97 ± 0.09** (6)*	3.39 ± 0.18 (6)	4.91 ± 0.41 (5)	3.34 ± 0.20 (6)	4.12 ± 0.47 (5)	**3.86 ± 0.50** (4)*	3.58 ± 0.23 (6)
Glutamate (Glu)	7.95 ± 0.51 (4)	9.29 ± 0.33 (5)	9.47 ± 0.57 (5)	7.41 ± 0.17 (5)	8.52 ± 0.26 (7)	8.98 ± 0.44 (6)	8.52 ± 0.43 (6)	10.36 ± 0.48 (5)	8.78 ± 0.45 (6)	9.41 ± 0.58 (5)	9.74 ± 0.21 (4)	8.94 ± 0.22 (6)
Glu/Gln	3.00 ± 0.28 (4)	2.81 ± 0.19 (5)	3.33 ± 0.50 (5)	**2.13 ± 0.15** (4)**	**2.05 ± 0.11** (7)*	**2.26 ± 0.12** (6) **	2.57 ± 0.24 (6)	2.19 ± 0.25 (5)	2.67 ± 0.19 (6)	2.39 ± 0.24 (5)	2.68 ± 0.40 (4)	2.42 ± 0.20 (6)
Glutathione	2.29 ± 0.14 (5)	2.43 ± 0.04 (5)	2.62 ± 0.21 (5)	2.20 ± 0.23 (7)	1.99 ± 0.21 (7)	**2.07 ± 0.15** (7)*	2.40 ± 0.17 (6)	2.72 ± 0.26 (5)	1.95 ± 0.25 (6)	2.79 ± 0.26 (5)	2.10 ± 0.33 (5)	2.14 ± 0.15 (6)
GPC + PCh	1.53 ± 0.15 (4)	1.53 ± 0.06 (5)	1.71 ± 0.07 (5)	1.40 ± 0.11 (5)	1.53 ± 0.07 (7)	1.65 ± 0.10 (6)	1.72 ± 0.08 (6)	1.72 ± 0.16 (5)	1.57 ± 0.12 (6)	1.78 ± 0.08 (5)	1.80 ± 0.09 (5)	1.58 ± 0.06 (6)
Inositol	2.47 ± 0.25 (3)	3.12 ± 0.20 (5)	3.46 ± 0.43 (5)	2.19 ± 0.35 (4)	2.84 ± 0.22 (7)	3.31 ± 0.34 (6)	4.65 ± 0.23 (6)	4.26 ± 0.62 (5)	4.30 ± 0.44 (6)	5.80 ± 0.37 (5) $p = 0.0776$	4.25 ± 0.36 (5)	4.57 ± 0.46 (6)
NAA	5.55 ± 0.20 (4)	6.47 ± 0.42 (5)	7.17 ± 0.43 (5)	5.63 ± 0.23 (6)	6.51 ± 0.27 (6)	6.67 ± 0.37 (7)	7.37 ± 0.31 (6)	6.80 ± 0.28 (5)	7.05 ± 0.22 (6)	8.30 ± 0.76 (5)	7.22 ± 0.89 (5)	7.26 ± 0.21 (6)
NAA + NAAG	5.78 ± 0.20 (5)	6.97 ± 0.28 (5)	8.20 ± 0.39 (5)	6.01 ± 0.12 (7)	7.04 ± 0.29 (7)	7.62 ± 0.26 (7)	7.53 ± 0.27 (6)	8.58 ± 0.27 (5)	7.73 ± 0.37 (6)	8.31 ± 0.76 (5)	8.23 ± 0.79 (5)	7.70 ± 0.22 (6)
PCr	7.26 ± 0.44 (5)	6.28 ± 0.36 (5)	6.96 ± 0.52 (4)	**4.73 ± 0.34** (6) ***	5.20 ± 0.66 (6)	**4.82 ± 0.29** (4) **	6.73 ± 0.57 (6)	4.60 ± 1.31 (4)	5.09 ± 0.54 (6)	8.17 ± 0.72 (6)	3.37 ± 0.68 (4)	4.65 ± 0.68 (6)
Taurine	8.02 ± 0.83 (5)	7.98 ± 0.43 (5)	8.49 ± 0.87 (5)	8.84 ± 0.81 (7)	9.10 ± 0.38 (7)	8.68 ± 0.55 (7)	8.21 ± 0.30 (6)	7.29 ± 0.15 (5)	8.33 ± 0.75 (6)	10.06 ± 0.83 (5) $p = 0.0515$	7.79 ± 0.36 (4)	9.13 ± 0.79 (6)

(Mean ± SEM; Two-way repeated measures ANOVA or Mixed-Model Analysis, Fisher post-hoc; * p value <0.05; ** p value <0.01; *** p value <0.001).

Table 6
Most relevant features characterizing the *Mecp2* deficient brain.

	Male				Female			
	P20 (no overt symptoms)		P40 (fully symptomatic)		P60 (no overt symptoms)		P200 (fully symptomatic)	
	KO	KI	KO	KI	HET	KI	HET	KI
MRI results								
Brain volume reduction	-	-	+	+	+	+	+	+
Cerebral cortex reduction	-	+/-[1]	+	+	+	+	+	+
Prefrontal c.	-	-	-	+	-	-	+	+
Entorhinal c.	-	-	+	+	+	-	+	+
Somatomotor c.	-	+	+	+	-	-	+	+
Somatosensory c.	-	-	+	+	-	+	+	+
Visual c.	-	-	+	+	-	+	+	+
Hippocampus reduction	+	+/-[2]	+	+	+	+	+	+
CA1	+	+	+	+	-	+	+	+
CA2	-	-	+	-	-	-	-	-
CA3	-	-	+	+	+	-	+	-
DG	+	+	+	+	-	-	+	-
Cerebellum reduction	-	-	+	-	-	-	-	+
Hypothalamus stagnation	n.a.	n.a.	+	+	n.a.	n.a.	+	
Cortical atrophy	n.a.	n.a.	-	VC	n.a.	n.a.	+	
Hippocampus atrophy	n.a.	n.a.	-	Regional	n.a.	n.a.	+	
MRS results								
Hippocampal GABA	-		+		-		-	
Hippocampal Glu/Gln	+		+		-		-	
Hippocampal PCr	+		+		-		-	
Hippocampal GSH	-		+		-		-	

n.a. not applicable; crossed boxes indicate not determined value; VC present in visual cortex. [1]p value 0,053; [2]p value 0,059.

5. Material and methods

5.1. Animals

All procedures were accomplished in accordance with the European Community Council Directive 2010/63/UE for care and use of experimental animals with protocols approved by the Italian Government (decrees No. 210/2017-PR and 1172/2020-PR) and the Institutional Animal Care and Use Committee.

Mouse lines were housed in the animal facility of the San Raffaele Scientific Institute and University of Milan. The *Mecp2* null mouse strain was originally purchased from the Jackson Laboratories, while the *Mecp2* KI Y120D mouse line was generated in our laboratory as described in Gandaglia et al., 2019. Both mouse strains were originally generated on a C57BL/6 J background and then transferred on a CD1 genetic background as previously described (Cobolli Gigli et al., 2016; Gandaglia et al., 2019). Mice were housed in groups of five in Tecniplast cages, on a 12 h light/dark cycle in a temperature-controlled environment (21 ± 2 °C) with food and water provided *ad libitum*.

Mouse genotypes were analyzed by PCR on genomic DNA purified from ears, as previously described (Cobolli Gigli et al., 2016, Gandaglia et al., 2019). The presence of RTT-like symptoms was evaluated following a well-established scoring system (Cobolli Gigli et al., 2016).

5.2. Magnetic resonance imaging

MRI experiments were conducted on a 7-Tesla scanner for rodents, fully equipped for brain MRI/MRS (Biospec, Paravision 6.0 Software Bruker-Biospin). A dedicated mouse head coil (4-channels) was used as receiver together with a volume coil as transmitter. A mixture of IsoVet (isoflurane 1–2%; Zootecnica, #104331020) with oxygen was used to anaesthetize animals and breath rate was constantly monitored to regulate the level of anaesthesia. Since IsoVet is an inhalation anaesthetic frequently used for general anaesthesia in animals, the induction and recovery from anaesthesia are rapid. Body temperature was maintained through warm water circulating inside the bed.

For cerebral anatomy analysis, T2-weighted images were acquired with a fast-spin-echo sequence (TR/TE = 3350–3500/44–45 ms, resolution of 73–76 μm, thickness of 0.65–0.7 mm, 9 averages, 9–12 min of acquisition). For the *Mecp2*$^{tm1.1Bird}$ line, the following littermate mice were used: $n = 7$ *Mecp2* null males; $n = 5$ WT males; $n = 6$ *Mecp2* HET females and n = 6 WT females. For the *Mecp2* Y120D line, we used: n = 6 *Mecp2* KI males; n = 5 WT males; n = 6 HET and WT females.

T2-weighted images were analyzed using a MATLAB toolbox, the Atlas Normalization Toolbox using elasti X (ANTX, https://github.com/ChariteExpMri/antx2), allowing to extract the cerebral volume of different brain areas following the Allen Mouse Brain Atlas (http://mouse.brain-map.org/). Areas with a cluster of at least 5 voxels were considered that correspond to a minimum volume >0.018 mm^3. Single brain region volume was then compared to the total brain volume of each mouse. The whole procedure was completed following the guidelines described in Koch et al. (2019). Animals whose fitting in the segmentation was not optimal were excluded from the analysis ($n = 1$ *Mecp2* null at P20 and n = 1 *Mecp2*$^{+/-}$ at P90 for the *Mecp2*$^{tm1.1Bird}$ line; n = 1 WT female at P200 and n = 1 HET female at P200 for the *Mecp2* Y120D line). In addition, because of technical issues during acquisition, the following female mice, belonging to the *Mecp2* Y120D line, were not included in the analysis: 1 WT at P60; 2 HET at P60; 2 WT at P200; and 1 KI at P200).

5.3. Magnetic resonance spectroscopy (^{1}H-MRS)

At the indicated ages, cerebral metabolites were measured *in vivo* using ^{1}H-MRS. A PRESS sequence (TR/TE = 2000/16.1 ms) was used with the selection of a voxel in different cerebral areas: the hippocampus (3.96–4.96 mm^3) and the cerebellum (9.72 mm^3) with water-suppression (VAPOR). The signal was accumulated 200–400 times according to the brain region (7–13 min of acquisition). For each area, magnetic field homogeneity was optimized using automatic map-shim calculation from a B0 map initially acquired. A spectrum without water suppression was also acquired and used as internal reference for metabolite concentration calculation using the LCModel program (http://s-provencher.com/lcmodel.shtml)(Provencher, 2001).

All acquired spectra were obtained with a suitable signal to noise ratio allowing the quantification of >12 metabolites. Metabolites with an estimated standard deviation (Cramer-Rao lower bounds, % SD) higher than 27% were excluded.

5.4. Brain sections and staining

Mice previously used for MRI experiments were included in molecular studies. Animals were anaesthetized by intraperitoneal injections of Tribromoethanol (250 mg/Kg) and transcardially perfused with 4% paraformaldehyde in PBS. Brains were removed and post-fixed in 4% paraformaldehyde overnight at 4 °C. Then, they were slowly dehydrated in 30% sucrose in PBS at 4 °C (48 h), frozen in isopentane at −30 °C for 3 min and stored at −80 °C. Each brain was embedded by PolyFreeze Tissue Freezing Medium (P0091, Merck, Darmstadt, Germany) and brain coronal sections (thickness 40 μm) were obtained with a cryostat (CM1860, Leica Biosystems, Wetzlar, Germany) and stored at −20 °C until staining.

Nissl staining was performed on at least three non-consecutive sections for each animal and three animals per group were analyzed and images acquired at 10× magnification with a Nikon Eclipse Ts2 inverted microscope equipped with a DS-Fi3 color microscope camera.

Immunofluorescence for phospho-rpS6 was performed on at least three non-consecutive sections for each animal and three animals per group were analyzed. Free-floating sections were permeabilized using 0.4% Triton X-100 in PBS for 30 min at 4 °C and blocked with 4% FBS and 0.1% Triton X-100 in PBS for 15 min at 4 °C. Sections were incubated with the primary antibody for rp-S6 (1:400; anti-phospho-S6 Ribosomal Protein (Ser240/244) antibody, Cod.2215, Cell Signaling) in blocking solution overnight at 4 °C. Then, sections were washed in PBS and incubated with Alexa Fluor anti-rabbit 568 conjugated secondary antibody (1:500; Cod. A11036, Thermo Fisher Scientific) in blocking solution for 1 h in the dark. After several washes in PBS (at least five washes of 5 min), DNA was stained with DAPI solution (1:1000 in PBS; Cod. 62,248, Thermo Fisher Scientific) following a 10 min incubation and sections were washed in PBS. Lastly, they were mounted on microscope slides with Fluoromount Aqueous Mounting Medium (Cod. F4680, Merck). Images were acquired at 20× magnification with a Nikon Eclipse Ni—U epi-fluorescence microscope. Immunofluorescence signal of phospho-rpS6 was analyzed by using Fiji software. In detail, a ROI was designed within the cerebral region of interest and maintained constant in size and position for all slices and animals. Integrated density was measured, and the values were percentualized on WT mice of the same brain area and age and then plotted on graph. All imaging analyses were performed by a researcher blind to the genotype.

5.5. Statistical analysis

Before any statistical analysis, normal distribution of data was assessed by applying the D'Agostino-Pearson normality test. In accordance with data distribution, statistical significance for multiple group comparisons was determined by Two-Way Analysis of Variance (ANOVA) followed by *post hoc* tests. Mixed effect model followed by *post hoc* tests was applied when missing values were present (values were above the stated cut-off or animals could not be considered for technical reasons). Unpaired student's *t*-test was used to compare immunofluorescence data in WT and HET samples. Statistically significance was expressed as: $*p < 0.05$; $**p < 0.01$; $***p < 0.001$; $****p < 0.0001$ and all the reported data were expressed as mean ± SEM. Statistical analyses

were performed using Prism 9 (GraphPad Software, CA). Error bar is represented in each figure, although in few of them values are too small to be graphically visible.

Funding

The project granted by Fondazione Roche to A.F. supported this work. G.D.R and E.A salaries were supported by the PhD program in Experimental Medicine, University of Milan. Salaries of S.C. and I.S. were supported by the International PhD course in Molecular Medicine, Università Vita-Salute San Raffaele. The authors acknowledge support from the University of Milan through the APC initiative. We are also extremely grateful to the Italian parents' association ProRETT Ricerca which supported part of the MRI costs.

Author contribution

S.C. and L.C. performed MRI and MRS experiments, contributed to the conceptual design of the project, analyzed and interpreted the data, and edited the manuscript. G.D.R. and E.A. performed histological and immunofluorescence analyses; G.D.R. also edited the text. I.S. and S.C.[#] performed molecular studies aimed at investigating the molecular causes of atrophy in the HET brain. P.B. supported the statistical analysis of MRS data. A.F. financially supported the study and edited the manuscript. N.L. directed the study, interpreted data, contributed to the conceptual design of the project and its financial support, wrote the first draft of the manuscript and edited the manuscript.

Conflict of interest

S.C., L.C., G.D., E.A., I.S., S.C.[#], P.B., A.F. and N.L. have no competing interest to declare.

Data availability

Data will be made available on request.

Acknowledgments

We are grateful to Tamara Canu and Antonio Esposito, MD, PhD, (Center of Experimental Imaging, CIS, part of the Italian Molecular Imaging node of Euro-BioImaging, www.eurobioimaging.eu) for access and excellent technical support for the 7-T MRI scanner. We thank Aurora Maria Natalia Mustaccia for her technical assistance. We wish to thank Dr. Philipp Boehm-Sturm from Charité (university of Berlin) for introducing the use of ANTx.

Appendix A. Supplementary data

Supplementary data to this article can be found online at https://doi.org/10.1016/j.nbd.2023.106083.

References

Achilly, N.P., He, L.J., Kim, O.A., Ohmae, S., Wojaczynski, G.J., Lin, T., Sillitoe, R.V., Medina, J.F., Zoghbi, H.Y., 2021. Deleting *Mecp2* from the cerebellum rather than its neuronal subtypes causes a delay in motor learning in mice. Elife. 10 https://doi.org/10.7554/eLife.64833 e64833. Jan 26. PMID: 33494858; PMCID: PMC7837679.

Akaba, Y., Shiohama, T., Komaki, Y., Seki, F., Ortug, A., Sawada, D., Uchida, W., Kamagata, K., Shimoji, K., Aoki, S., Takahashi, S., Suzuki, T., Natsume, J., Takahashi, E., Tsujimura, K., 2022. Comprehensive volumetric analysis of *Mecp2*-null mouse model for Rett syndrome by T2-weighted 3D magnetic resonance imaging. Front. Neurosci. 16 https://doi.org/10.3389/fnins.2022.885335, 885335. May 10. PMID: 35620663; PMCID: PMC9127869.

Allemang-Grand, R., Ellegood, J., Spencer Noakes, L., Ruston, J., Justice, M., Nieman, B. J., Lerch, J.P., 2017. Neuroanatomy in mouse models of Rett syndrome is related to the severity of Mecp2 mutation and behavioral phenotypes. Mol. Autism. 8, 32. https://doi.org/10.1186/s13229-017-0138-8. Jun 26. PMID: 28670438; PMCID: PMC5485541.

Armstrong, D.D., 2001. Rett syndrome neuropathology review 2000. Brain and Development 23 (Suppl. 1), S72–S76. https://doi.org/10.1016/s0387-7604(01)00332-1. Dec. (PMID: 11738845).

Asaka, Y., Jugloff, D.G., Zhang, L., Eubanks, J.H., Fitzsimonds, R.M., 2006. Hippocampal synaptic plasticity is impaired in the Mecp2-null mouse model of Rett syndrome. Neurobiol. Dis. 21 (1), 217–227. https://doi.org/10.1016/j.nbd.2005.07.005. Jan. Epub 2005 Aug 8. PMID: 16087343.

Bedogni, F., Rossi, R.L., Galli, F., Cobolli Gigli, C., Gandaglia, A., Kilstrup-Nielsen, C., Landsberger, N., 2014. Rett syndrome and the urge of novel approaches to study MeCP2 functions and mechanisms of action. Neurosci. Biobehav. Rev. 46 (Pt 2), 187–201. https://doi.org/10.1016/j.neubiorev.2014.01.011. Oct. Epub 2014 Mar 2. PMID: 24594195.

Bedogni, F., Cobolli Gigli, C., Pozzi, D., Rossi, R.L., Scaramuzza, L., Rossetti, G., Pagani, M., Kilstrup-Nielsen, C., Matteoli, M., Landsberger, N., 2016. Defects during Mecp2 null embryonic cortex development precede the onset of overt neurological symptoms. Cereb. Cortex 26 (6), 2517–2529. https://doi.org/10.1093/cercor/bhv078. Jun. Epub 2015 May 15. PMID: 25979088.

Belichenko, P.V., Wright, E.E., Belichenko, N.P., Masliah, E., Li, H.H., Mobley, W.C., Francke, U., 2009. Widespread changes in dendritic and axonal morphology in Mecp2-mutant mouse models of Rett syndrome: evidence for disruption of neuronal networks. J. Comp. Neurol. 514 (3), 240–258. https://doi.org/10.1002/cne.22009. May 20. (PMID: 19296534).

Borloz, E., Villard, L., Roux, J.C., 2021. Rett syndrome: think outside the (skull) box. Fac Rev. 10, 59. https://doi.org/10.12703/r/10-59. Jun 29. PMID: 34308425; PMCID: PMC8265562.

Calfa, G., Percy, A.K., Pozzo-Miller, L., 2011. Experimental models of Rett syndrome based on Mecp2 dysfunction. Exp. Biol. Med. (Maywood) 236 (1), 3–19. https://doi.org/10.1258/ebm.2010.010261. Jan. PMID: 21239731; PMCID: PMC3059199.

Cobolli Gigli, C., Scaramuzza, L., Gandaglia, A., Bellini, E., Gabaglio, M., Parolaro, D., Kilstrup-Nielsen, C., Landsberger, N., Bedogni, F., 2016. MeCP2 related studies benefit from the use of CD1 as genetic background. PLoS One 11 (4). https://doi.org/10.1371/journal.pone.0153473 e0153473. Apr 20. PMID: 27097329; PMCID: PMC4838291.

Cosentino, L., Vigli, D., Franchi, F., Laviola, G., De Filippis, B., 2019. Rett syndrome before regression: a time window of overlooked opportunities for diagnosis and intervention. Neurosci. Biobehav. Rev. 107, 115–135. https://doi.org/10.1016/j.neubiorev.2019.05.013. Dec. Epub 2019 May 18. PMID: 31108160.

Frasca, A., Kilstrup, Nielsen C., Landsberger, N., 2023. Chapter 6 - Rett syndrome: from the involved gene(s) to treatment. In: Zigmond, Michael J., Wiley, Clayton A., Chesselet, Marie-Francoise (Eds.), Neurobiology of Brain Disorders, Second edition. Academic Press, pp. 89–113. ISBN 9780323856546. https://doi.org/10.1016/B978-0-323-85654-6.00002-2.

Fyffe, S.L., Neul, J.L., Samaco, R.C., Chao, H.T., Ben-Shachar, S., Moretti, P., McGill, B.E., Goulding, E.H., Sullivan, E., Tecott, L.H., Zoghbi, H.Y., 2008. Deletion of Mecp2 in Sim1-expressing neurons reveals a critical role for MeCP2 in feeding behavior, aggression, and the response to stress. Neuron. 59 (6), 947–958. https://doi.org/10.1016/j.neuron.2008.07.030. Sep 25. PMID: 18817733; PMCID: PMC2597031.

Gandaglia, A., Brivio, E., Carli, S., Palmieri, M., Bedogni, F., Stefanelli, G., Bergo, A., Leva, B., Cattaneo, C., Pizzamiglio, L., Cicerone, M., Bianchi, V., Kilstrup-Nielsen, C., D'Annessa, I., Di Marino, D., D'Adamo, P., Antonucci, F., Frasca, A., Landsberger, N., 2019. A novel Mecp2^{Y120D} knock-in model displays similar behavioral traits but distinct molecular features compared to the Mecp2-null mouse implying precision medicine for the treatment of Rett syndrome. Mol. Neurobiol. 56 (7), 4838–4854. https://doi.org/10.1007/s12035-018-1412-2. Jul. Epub 2018 Nov 6. PMID: 30402709.

Guy, J., Hendrich, B., Holmes, M., Martin, J.E., Bird, A., 2001. A mouse Mecp2-null mutation causes neurological symptoms that mimic Rett syndrome. Nat. Genet. 27 (3), 322–326. https://doi.org/10.1038/85899. Mar. (PMID: 11242117).

Koch, S., Mueller, S., Foddis, M., Bienert, T., von Elverfeldt, D., Knab, F., et al., 2019. Atlas registration for edema-corrected MRI lesion volume in mouse stroke models. J. Cereb. Blood Flow Metab. 39, 313–323. https://doi.org/10.1177/0271678x17726635.

Kuijpers, M., 2022. Keeping synapses in shape: degradation pathways in the healthy and aging brain. Neuronal Signal 6 (2). https://doi.org/10.1042/NS20210063. NS20210063. Jun 15. PMID: 35813265; PMCID: PMC9208270.

Lombardi, L.M., Baker, S.A., Zoghbi, H.Y., 2015. MECP2 disorders: from the clinic to mice and back. J. Clin. Invest. 125 (8), 2914–2923. https://doi.org/10.1172/JCI78167. Aug 3. Epub 2015 Aug 3. PMID: 26237041; PMCID: PMC4563741.

Mahmood, A., Bibat, G., Zhan, A.L., Izbudak, I., Farage, L., Horska, A., Mori, S., Naidu, S., 2010. White matter impairment in Rett syndrome: diffusion tensor imaging study with clinical correlations. AJNR Am. J. Neuroradiol. 31 (2), 295–299. https://doi.org/10.3174/ajnr.A1792. Feb. Epub 2009 Oct 15. PMID: 19833797; PMCID: PMC2909097.

Marschik, P.B., Kaufmann, W.E., Sigafoos, J., Wolin, T., Zhang, D., Bartl-Pokorny, K.D., Pini, G., Zappella, M., Tager-Flusberg, H., Einspieler, C., Johnston, M.V., 2013. Changing the perspective on early development of Rett syndrome. Res. Dev. Disabil. 34 (4), 1236–1239. https://doi.org/10.1016/j.ridd.2013.01.014. Apr. Epub 2013 Feb 9. PMID: 23400005; PMCID: PMC3605580.

Neul, J.L., Kaufmann, W.E., Glaze, D.G., Christodoulou, J., Clarke, A.J., Bahi-Buisson, N., Leonard, H., Bailey, M.E., Schanen, N.C., Zappella, M., Renieri, A., Huppke, P., Percy, A.K., RettSearch Consortium, 2010. Rett syndrome: revised diagnostic criteria and nomenclature. Ann. Neurol. 68 (6), 944–950. https://doi.org/10.1002/ana.22124. Dec. (PMID: 21154482; PMCID: PMC3058521).

Provencher, S.W., 2001. Automatic quantitation of localized in vivo 1H spectra with LCModel. NMR Biomed. 14 (4), 260–264. https://doi.org/10.1002/nbm.698. Jun. (PMID: 11410943).

Ricciardi, S., Boggio, E.M., Grosso, S., Lonetti, G., Forlani, G., Stefanelli, G., Calcagno, E., Morello, N., Landsberger, N., Biffo, S., Pizzorusso, T., Giustetto, M., Broccoli, V., 2011. Reduced AKT/mTOR signaling and protein synthesis dysregulation in a Rett syndrome animal model. Hum. Mol. Genet. 20 (6), 1182–1196. https://doi.org/10.1093/hmg/ddq563. Mar 15. Epub 2011 Jan 6. PMID: 21212100.

Saywell, V., Viola, A., Confort-Gouny, S., Le Fur, Y., Villard, L., Cozzone, P.J., 2006. Brain magnetic resonance study of Mecp2 deletion effects on anatomy and metabolism. Biochem. Biophys. Res. Commun. 340 (3), 776–783. https://doi.org/10.1016/j.bbrc.2005.12.080. Feb 17. Epub 2005 Dec 20. PMID: 16380085.

Schimanski, L.A., Barnes, C.A., 2010. Neural protein synthesis during aging: effects on plasticity and memory. Front. Aging Neurosci. 2, 26. https://doi.org/10.3389/fnagi.2010.00026. Aug 6. PMID: 20802800; PMCID: PMC2928699.

Shahbazian, M., Young, J., Yuva-Paylor, L., Spencer, C., Antalffy, B., Noebels, J., Armstrong, D., Paylor, R., Zoghbi, H., 2002. Mice with truncated MeCP2 recapitulate many Rett syndrome features and display hyperacetylation of histone H3. Neuron. 35 (2), 243–254. https://doi.org/10.1016/s0896-6273(02)00768-7. Jul 18. (PMID: 12160743).

Shiohama, T., Levman, J., Takahashi, E., 2019. Surface- and voxel-based brain morphologic study in Rett and Rett-like syndrome with MECP2 mutation. Int. J. Dev. Neurosci. 73, 83–88. https://doi.org/10.1016/j.ijdevneu.2019.01.005. Apr. Epub 2019 Jan 25. PMID: 30690146; PMCID: PMC6377336.

Shovlin, S., Tropea, D., 2018. Transcriptome level analysis in Rett syndrome using human samples from different tissues. Orphanet J. Rare Dis. 13 (1), 113. https://doi.org/10.1186/s13023-018-0857-8. Jul 11. PMID: 29996871; PMCID: PMC6042368.

Squillaro, T., Alessio, N., Cipollaro, M., Melone, M.A., Hayek, G., Renieri, A., Giordano, A., Galderisi, U., 2012. Reduced expression of MECP2 affects cell commitment and maintenance in neurons by triggering senescence: new perspective for Rett syndrome. Mol. Biol. Cell 23 (8), 1435–1445. https://doi.org/10.1091/mbc.E11-09-0784. Apr. Epub 2012 Feb 22. PMID: 22357617; PMCID: PMC3327309.

Stearns, N.A., Schaevitz, L.R., Bowling, H., Nag, N., Berger, U.V., Berger-Sweeney, J., 2007. Behavioral and anatomical abnormalities in Mecp2 mutant mice: a model for Rett syndrome. Neuroscience. 146 (3), 907–921. https://doi.org/10.1016/j.neuroscience.2007.02.009. May 25. Epub 2007 Mar 23. PMID: 17383101.

Ward, B.C., Agarwal, S., Wang, K., Berger-Sweeney, J., Kolodny, N.H., 2008. Longitudinal brain MRI study in a mouse model of Rett syndrome and the effects of choline. Neurobiol. Dis. 31 (1), 110–119. https://doi.org/10.1016/j.nbd.2008.03.009. Jul. Epub 2008 Apr 10. PMID: 18571096.

Ward, B.C., Kolodny, N.H., Nag, N., Berger-Sweeney, J.E., 2009. Neurochemical changes in a mouse model of Rett syndrome: changes over time and in response to perinatal choline nutritional supplementation. J. Neurochem. 108 (2), 361–371. https://doi.org/10.1111/j.1471-4159.2008.05768.x. Jan. Epub 2008 Nov 6. PMID: 19012748.

Ip, J.P.K., Mellios, N., Sur, M., 2018. Rett syndrome: insights into genetic, molecular and circuit mechanisms. Nat Rev Neurosci 19 (6), 368–382. https://doi.org/10.1038/s41583-018-0006-3. PMID: 29740174; PMCID: PMC6402579.